

¹ **Large Eddy Simulations of Stabilizing Effects Induced by Opposing Eulerian
2 Shear and Stokes Drift Shear in an Idealized Ocean Surface Boundary Layer**

³ Qing Li^{a,b}

⁴ *^a Earth, Ocean and Atmospheric Sciences Thrust, The Hong Kong University of Science and
5 Technology (Guangzhou), Guangzhou, Guangdong, China*

⁶ *^b Center for Ocean Research in Hong Kong and Macau, The Hong Kong University of Science
7 and Technology, Hong Kong, China*

⁸ Corresponding author: Qing Li, ocqingli@hkust-gz.edu.cn

9 ABSTRACT: Ocean surface waves strongly modulate vertical turbulent mixing in the ocean surface
10 boundary layer. When they are aligned with wind-driven Eulerian shear, Craik-Leibovich instability
11 occurs, resulting in the formation of Langmuir turbulence that strongly enhances vertical mixing.
12 By the same mechanism, ocean surface waves can also stabilize the water column and suppress
13 boundary layer turbulence when they are in opposite direction as the Eulerian shear. Here, we
14 demonstrate this stabilizing effect induced by opposing Eulerian shear and Stokes drift shear in large
15 eddy simulations (LES) under idealized homogeneous surface cooling and no-wind conditions.
16 Rolls of convection form under the competing effects of destabilizing surface cooling and stabilizing
17 wave-induced stratification. The latter depends on the alignment of Eulerian shear and Stokes
18 drift shear, resulting in roll structures aligned perpendicular to Stokes drift. In addition, the
19 intensity of turbulence is significantly reduced as compared to the case of pure convection. Such
20 stabilizing effect of wave-induced stratification has yet to be incorporated in wave-driven mixing
21 parameterizations and may lead to potential improvements. Using this idealized test case, we also
22 demonstrate the effect of assuming down-Eulerian shear mixing versus down-Lagrangian shear
23 mixing in the sub-grid scale scheme by comparing two LES models. While such effect may be
24 hidden in strongly wind-forced cases, it results in completely different solutions in this idealized
25 case by changing the boundary condition for the mean flow. Therefore, care should be taken when
26 designing and interpreting LES with misaligned currents and waves.

27 **1. Introduction**

28 It has long been well recognized that the presence of surface gravity waves enhances vertical
29 turbulent mixing in the ocean surface boundary layer by generating Langmuir turbulence (Leibovich
30 1983; Thorpe 2004; Sullivan and McWilliams 2010; D’Asaro 2014). The resulting turbulence
31 structure, characterized by pairs of vortex tubes parallel to the direction of wind and waves, is
32 distinct from the streaky structure of wind-driven shear turbulence and downwelling plumes of
33 convective turbulence (e.g., McWilliams et al. 1997; Li et al. 2005; Teixeira 2011). The Craik-
34 Leibovich (CL) theory (Craik and Leibovich 1976; Leibovich 1983), in particular the CL type
35 2 instability that involves the vertical shear of Stokes drift, is the main mechanism driving the
36 Langmuir turbulence. For inviscid neutrally stratified flow, the criterion for instability is that
37 the vertical shear of the mean Eulerian current is aligned with the vertical shear of Stokes drift
38 (Leibovich 1977). This condition is often satisfied in a typical wind-driven ocean surface boundary
39 layer in the presence of wind waves. Large eddy simulations (LES) that solve the CL equation
40 have been shown to reproduce the higher vertical velocity variance observed in lakes and open
41 oceans (e.g., D’Asaro et al. 2014) and more rapid deepening of the mixed layer (e.g., Kukulka et al.
42 2009) when waves are present. Such effects have been incorporated into different turbulent mixing
43 parameterizations of the ocean surface boundary layer (Li et al. 2019), which generally improve
44 the performance of ocean general circulation models (e.g., Fan and Griffies 2014; Li et al. 2016).

45 However, the presence of surface gravity waves may also suppress vertical turbulent mixing by
46 the same mechanism under relatively rare but possible conditions when the Eulerian shear opposes
47 the Stokes drift shear (Leibovich 1977, 1983). Indications of such an effect can be found in the
48 LESs of Langmuir turbulence for misaligned winds and waves by Van Roekel et al. (2012), which
49 show a slightly weaker vertical velocity variance than the shear-only case when the angle between
50 the wind and wave reaches 135° (their Figure 3). They are also apparent in the LESs of Langmuir
51 turbulence in swell by McWilliams et al. (2014), in which turbulent viscosity was found to decrease
52 when swell-waves of increasing amplitude are added to an equilibrium wind-wave driven boundary
53 layer (their Figure 6) and vertical velocity variance decreases with decreasing Langmuir number in
54 weak wind conditions (their Figure 8). The stabilizing effect induced by opposing Eulerian shear
55 and Stokes drift shear is also suggested in the modified criterion for symmetric instability influenced
56 by ocean surface waves as explored in detail in Haney et al. (2015). This stabilizing effect could

therefore be as important as its destabilizing counterpart, which drives Langmuir turbulence, in causing the anisotropy of frontal strength in a submesoscale frontal spindown simulation in the presence of Stokes forces (Hamlington et al. 2014; Suzuki et al. 2016). In general, this stabilizing effect has received much less attention than its destabilizing counterpart. And aside from the second-moment closure model of Langmuir turbulence by Harcourt (2013) and maybe a somewhat implicit representation in the scaling of vertical velocity variance in Van Roekel et al. (2012), such a stabilizing effect is often ignored in turbulent mixing parameterizations of the ocean surface boundary layer that include the effects of surface gravity waves (Li et al. 2019).

The first goal of this paper is to demonstrate the stabilizing effect induced by opposing Eulerian shear and Stokes drift shear on the intensity and structures of boundary layer turbulence in a clean way. For this purpose, an idealized case can be used, starting from an initial mixed layer with zero Lagrangian velocity and forced by steady and homogeneous surface cooling and zero wind stress. While the applicability of these extremely idealized conditions in real-world scenarios and their implications deserves some discussion (deferred to Section 6), they certainly make it much easier for demonstration. Ideally, the flow should be turbulent to counteract the stabilizing effect of waves, and the condition of opposing Eulerian shear and Stokes drift shear should be maintained. In the idealized case here, the surface cooling serves as a source of turbulence, and the no-wind condition ensures that no significant Lagrangian flow is introduced. As will be shown later, this combination of initial condition and surface forcing provides favorable conditions for the competition between destabilizing surface cooling and stabilizing wave-induced stratification, and promotes the emergence of interesting turbulence structures.

LES that solves the CL equation has become an essential tool for studying ocean surface boundary layer turbulence under the influence of ocean surface waves (e.g., McWilliams et al. 1997; Li et al. 2005; Grant and Belcher 2009; Harcourt and D’Asaro 2008; Van Roekel et al. 2012; Hamlington et al. 2014; McWilliams et al. 2014; Li and Fox-Kemper 2017; Wagner et al. 2021). However, there are practical issues in solving the CL equation using the LES technique. For example, the presence of ocean surface waves changes the anisotropy of turbulence (Li et al. 2005; Li and Fox-Kemper 2020), which may affect the applicability of an isotropic Smagorinsky-type sub-grid scale (SGS) model (Sullivan et al. 1994). Artificial production of turbulent kinetic energy (TKE) induced by the turbulence-induced anti-Stokes flow may also arise in LES and depends on the SGS model

(Pearson 2018). A relevant question to ask is, then, to what extent can we trust the solutions of an LES? Validation against laboratory experiments and field observations is preferable, yet is limited by the relatively small amount of data available for the broad parameter space spanned in the ocean surface boundary layer. Intercomparison among models over a wide range of conditions (e.g., Beare et al. 2006; Fan et al. 2024) is also helpful in revealing potential uncertainties.

Therefore, another goal of this paper is to clarify the subtle differences between LES models introduced by adopting different formulations in their SGS model, specifically, the effect of assuming down-Eulerian shear mixing versus down-Lagrangian shear mixing. The idealized case mentioned above proves to be useful for this purpose. Ideally, such a comparison in the SGS model formulation should be done in the same numerical framework. However, the convenience of having two LES models at hand (NCAR LES and Oceananigans to be introduced in Section 3), adopting SGS models that assume down-Eulerian shear mixing and down-Lagrangian shear mixing, respectively, makes it much easier to compare the two LES models using the same test cases, rather than implementing an alternative SGS formulation in either model. In fact, the idealized test case presented in this paper is one of a larger set of test cases in an effort to compare these two LES models under various forcing conditions. And this paper was motivated by the intriguing fact that two LES models give completely different solutions in this seemingly straightforward test case.

The remainder of this paper is organized as follows. First, the stabilizing wave-induced stratification is analyzed from the perspective of a linear stability analysis around a baseline configuration of perfectly opposing Eulerian shear and Stokes drift shear (therefore zero Lagrangian shear) in Section 2. This provides a theoretical background for the turbulent structures expected in the LES. Section 3 describes the two LES models, Oceananigans and NCAR LES, and configurations of the test cases. The solution given by Oceananigans is presented in Section 4, which shows turbulent structures predicted by the linear stability analysis. A different solution is found in NCAR LES, which is presented in Section 5, together with an investigation of possible reasons for the differences and a reconciliation. Finally, this paper ends with some discussions on the implications for future studies in Section 6 and a brief summary in Section 7.

¹¹⁴ **2. Stabilizing Wave-Induced Stratification by Opposing Eulerian Shear and Stokes Drift**

¹¹⁵ **Shear**

¹¹⁶ The Craik-Leibovich (CL) equation (Craik and Leibovich 1976; Leibovich 1983) written in a
¹¹⁷ formulation with the Stokes shear force (Suzuki and Fox-Kemper 2016) is

$$\partial_t \mathbf{u} + (\mathbf{u}^L \cdot \nabla) \mathbf{u} = b \hat{\mathbf{z}} - \nabla \cdot \boldsymbol{\tau} - \nabla p - \mathbf{f} \times \mathbf{u}^L - u_j^L \nabla u_j^S, \quad (1)$$

¹¹⁸ where \mathbf{f} is the Coriolis parameter in its vector form, p is the kinematic pressure, b is the buoyancy
¹¹⁹ acting in the vertical direction indicated by a unit vector $\hat{\mathbf{z}}$, and $\boldsymbol{\tau}$ is the stress tensor. The Lagrangian
¹²⁰ velocity \mathbf{u}^L , Eulerian velocity \mathbf{u} and Stokes drift \mathbf{u}^S are linked by $\mathbf{u}^L = \mathbf{u} + \mathbf{u}^S$. The last term in (1)
¹²¹ is the Stokes shear force acting in the direction of the Stokes drift gradient. In index notation, this
¹²² term is written as $-u_j^L \partial_i u_j^S$. Incompressibility is enforced by

$$\nabla \cdot \mathbf{u} = 0, \quad (2)$$

¹²³ and we assume $\nabla \cdot \mathbf{u}^S = 0$. The buoyancy is advected by the Lagrangian velocity,

$$\partial_t b + (\mathbf{u}^L \cdot \nabla) b = -\nabla \cdot q_b, \quad (3)$$

¹²⁴ where q_b is a diffusive flux of buoyancy. There are other mathematically equivalent formulations of
¹²⁵ the CL equation (see, e.g., Holm 1996; Suzuki and Fox-Kemper 2016), each having its advantages
¹²⁶ that emphasize different aspects of the dynamics. Here, we use (1) for its intuitive physical picture.

¹²⁷ A linear instability analysis is conducted on (1) to demonstrate the stabilizing wave-induced
¹²⁸ stratification (Leibovich 1977; Bühler 2014) induced by an Eulerian current exactly opposing the
¹²⁹ Stokes drift (such that $\mathbf{u}^L = 0$). Consider a simple case with horizontally homogeneous Stokes drift
¹³⁰ that decays with depth ($\mathbf{u}^S = [u^S(z), 0, 0]$) and ignore rotation ($\mathbf{f} = 0$) and diffusion ($\nabla \cdot \boldsymbol{\tau} = 0$ and
¹³¹ $\nabla \cdot q_b = 0$). The Stokes shear force due to the vertical shear of Stokes drift appears only in the
¹³² vertical momentum equation. Now we linearize (1) and (3) around a horizontally homogeneous
¹³³ mean state such that $\mathbf{u} = [\bar{u}(z) + u', v', w']$, $b = \bar{b}(z) + b'$, and $p = \bar{p}(z) + p'$, assuming $|\bar{u}| \gg |u'|$,
¹³⁴ $|\bar{b}| \gg |b'|$, and $|\bar{p}| \gg |p'|$. Here, $\bar{(\cdot)}$ is the horizontal mean and $(\cdot)'$ is the fluctuations from the
¹³⁵ mean. The background Eulerian mean flow $\bar{u} = -u^S$ exactly counterbalances the Stokes drift so

136 that $\bar{u}^L = \bar{u} + u^S = 0$. The mean states (\bar{u} , \bar{b} and \bar{p}) are functions of z only (the wavy hydrostatic
 137 balance $\partial_z \bar{p} = \bar{b} - \bar{u}^L \partial_z u^S$ reduces to $\partial_z \bar{p} = \bar{b}$ given $\bar{u}^L = 0$), and the fluctuations on top depend on
 138 the location $[x, y, z]$ and time t . The linearized equations for the fluctuations, given the condition
 139 $\partial_z \bar{u} = -\partial_z u^S$, are then

$$\partial_t u' - w' \partial_z u^S = -\partial_x p', \quad (4)$$

$$\partial_t v' = -\partial_y p', \quad (5)$$

$$\partial_t w' = -\partial_z p' + b' - u' \partial_z u^S, \quad (6)$$

$$\partial_t b' + N^2 w' = 0, \quad (7)$$

140 where $N^2 = \partial_z \bar{b}$ is the mean stratification. Note that since \mathbf{u}^S is prescribed in the CL equation,
 141 $[u', v', w']$ can be viewed as fluctuations on either \mathbf{u} or \mathbf{u}^L , which does not affect the linearized
 142 equations (4)–(7). For simplicity, we assume that both N^2 and $\partial_z u^S$ are constant, so wave-
 143 like solutions of (4)–(7) in the form of $\lambda' = \hat{\lambda} \exp[i(k_x x + k_y y + k_z z - \omega t)]$ are sought. With
 144 general vertical profiles of N^2 and $\partial_z u^S$, one should not expect sinusoidal solution in the vertical.
 145 However, this assumption greatly simplifies the discussion here. With the continuity equation for
 146 the fluctuations,

$$\partial_x u' + \partial_y v' + \partial_z w' = 0, \quad (8)$$

147 existence of nontrivial solutions requires

$$\omega^2 = \frac{k_x^2 + k_y^2}{k_x^2 + k_y^2 + k_z^2} \left[N^2 + \frac{k_y^2}{k_x^2 + k_y^2} (\partial_z u^S)^2 \right]. \quad (9)$$

148 The second term in the brackets in (9) is non-negative. It represents a stabilizing wave-induced
 149 stratification by opposing Eulerian shear and Stokes drift shear (see more discussion on this analogy
 150 to stratification in Section 11.3.1 of Bühler 2014). The first term in the brackets represents the
 151 effect of a stabilizing or destabilizing stratification depending on the sign of N^2 . When $N^2 > 0$,
 152 the system is stable to all fluctuations ($\omega^2 > 0$). When $N^2 < 0$, gravitational instability may occur,
 153 but is modulated by the stabilizing wave-induced stratification. The most unstable fluctuations
 154 have the property of $k_x \gg k_y$. In other words, the stabilizing effect induced by opposing Eulerian
 155 shear and Stokes drift shear has a preference in directions. It tends to stabilize fluctuations in the

crosswise (y) direction (with higher wavenumber k_y). This contrasts to the stabilizing effect of positive N^2 , which has no preference in directions. Therefore, we expect the convective cells to align in the crosswise direction, perpendicular to the direction of Stokes drift (streamwise). As shown in Section 4, this is indeed the turbulence structure shown in the LES solutions when the condition $\partial_z \bar{u} = -\partial_z u^S$ is satisfied.

This directional preference for stabilizing wave-induced stratification can also be understood from the perspective of Stokes shear force (last term in (6)). For the condition considered here ($\partial_z \bar{u} = -\partial_z u^S < 0$), a water parcel moving downward ($w' < 0$) from its initial position carries a negative fluctuation in streamwise velocity ($u' < 0$) as compared to its surrounding environment (according to (4)). Then, according to (6), this water parcel experiences a positive Stokes shear force, which tends to return it to its initial position. This stabilizing restoring force is similar to the restoring buoyancy force experienced by a water parcel displaced vertically in a stable stratification. But unlike the oscillating water parcel under statically stable conditions, which goes up and down, the oscillation of the water parcel under the stabilizing Stokes shear force requires fluctuations in the streamwise velocity u' (thus oscillating in rolls). Fluctuations in the crosswise velocity v' will not generate such restoring force. This is similar to the directional preference for destabilizing effects in Langmuir turbulence when the Eulerian shear aligns with the Stokes drift shear (Leibovich 1977; Suzuki and Fox-Kemper 2016).

3. Large Eddy Simulations and Experiment Setup

Oceananigans (Ramadhan et al. 2020; Wagner et al. 2021) is a fast and user-friendly software package for numerical simulations of geophysical fluid dynamics written in the Julia programming language. It uses a finite-volume spatial discretization and can be configured as an LES with various combinations of SGS, advection and time-stepping schemes. In this study, we solve the Lagrangian formulation of the CL equation (e.g., Holm 1996),

$$\partial_t \mathbf{u}^L + (\mathbf{u}^L \cdot \nabla) \mathbf{u}^L = b \hat{\mathbf{z}} - \nabla \cdot \boldsymbol{\tau} - \nabla p - \mathbf{f} \times \mathbf{u}^L + (\nabla \times \mathbf{u}^S) \times \mathbf{u}^L + \partial_t \mathbf{u}^S, \quad (10)$$

using the anisotropic minimum dissipation closure (Rozema et al. 2015; Verstappen 2018) combined with the third-order Runge-Kutta timestepping and fifth-order WENO advection scheme. The initial and boundary conditions are applied on the Lagrangian field. Although relatively new,

183 it has already been used in simulating ocean boundary layer turbulence under various forcing
 184 conditions (e.g., Wagner et al. 2021, 2023; Wagner and Constantinou 2025; Huang et al. 2026; Wei
 185 et al. 2025). Unless otherwise noted, the solutions we present in this paper are from Oceananigans
 186 (v0.91.3).

187 By solving the Lagrangian velocity \mathbf{u}^L in (10), a down-Lagrangian shear mixing assumption is
 188 naturally adopted in the SGS model of Oceananigans (Wagner et al. 2021). In contrast, a down-
 189 Eulerian shear mixing assumption is commonly adopted in traditional LES models solving the
 190 Eulerian formulation of the CL equation,

$$\partial_t \mathbf{u} + (\mathbf{u} \cdot \nabla) \mathbf{u} = b \hat{\mathbf{z}} - \nabla \cdot \boldsymbol{\tau} - \nabla \left(p + \frac{1}{2} |\mathbf{u}^L|^2 - \frac{1}{2} |\mathbf{u}|^2 \right) - \mathbf{f} \times \mathbf{u}^L - (\nabla \times \mathbf{u}) \times \mathbf{u}^S. \quad (11)$$

191 Note that (10), (11), and (1) are mathematically equivalent (Holm 1996; Suzuki and Fox-Kemper
 192 2016), so the essential difference between Oceananigans and traditional LES models is in their
 193 SGS model. To demonstrate this difference, a popular LES model that solves (11), the NCAR LES
 194 (Moeng 1984; McWilliams et al. 1997), is used here. NCAR LES uses a modified Smagorinsky
 195 SGS closure that evolves a prognostic equation for the SGS TKE (Deardorff 1980; Sullivan et al.
 196 1994). The two-part SGS model described in Sullivan et al. (1994) to account for the turbulence
 197 anisotropy by strong shear near the surface is not used. The spatial discretization is pseudospectral
 198 in the horizontal and finite-difference in the vertical. It has been widely used by different groups
 199 in simulating Langmuir turbulence under various surface forcing conditions (e.g., McWilliams
 200 et al. 1997; Van Roekel et al. 2012; McWilliams et al. 2014; Li and Fox-Kemper 2017) and the
 201 interaction between boundary layer turbulence and submesoscale fronts (e.g., Hamlington et al.
 202 2014; Sullivan and McWilliams 2024).

203 In both Oceananigans and NCAR LES, we employ a steady Stokes drift profile for a monochro-
 204 matic wave of amplitude a and wavenumber k in the deep-water limit,

$$\mathbf{u}^S = u_0^S \exp(2kz) \hat{\mathbf{x}}, \quad (12)$$

205 where $u_0^S = a^2 k \sqrt{gk}$ is the surface Stokes drift, with g the gravitational acceleration. In the
 206 baseline configuration, we choose $a = 0.8$ m and $k = 2\pi/60 \approx 0.105$ m $^{-1}$, which corresponds to
 207 an e-folding depth of $1/2k \approx 4.8$ m for the decay of Stokes drift. To demonstrate wave-induced

stratification, we also vary the wave amplitude by choosing $a = [0.45, 0.8, 1.423]$ m while keeping the wavenumber k unchanged. This corresponds to a 10-fold change in the strength of wave-induced stratification $(\partial_z u^S)^2 \propto a^4$ at the same depth between successive wave configurations. These cases are respectively referred to as the “weak-wave”, “moderate-wave”, and “strong-wave” cases. We also include a “no-wave” case with $a = 0$ m as a reference.

Constant surface cooling is introduced in these experiments to generate turbulence that mixes into stabilizing wave-induced stratification. In the baseline configuration, we choose a surface cooling of $Q_0 = 50 \text{ W m}^{-2}$. We also vary the surface cooling by choosing $Q_0 = [5, 50, 500] \text{ W m}^{-2}$ to demonstrate its completion effects with stabilizing wave-induced stratification. The surface heat flux translates into the surface buoyancy flux $B_0 = \alpha g Q_0 / \rho_o c_p$ by setting the thermal expansion coefficient $\alpha = 2 \times 10^{-4} \text{ }^\circ\text{C}^{-1}$, density of seawater $\rho_o = 1026 \text{ kg m}^{-3}$, and specific heat of seawater $c_p = 3991 \text{ J kg}^{-1} \text{ }^\circ\text{C}^{-1}$.

The initial condition for the Lagrangian velocity is $\mathbf{u}^L|_{t=0} = 0$, implying an initial Eulerian velocity of $\mathbf{u}|_{t=0} = -\mathbf{u}^S$. The initial buoyancy field has a mixed layer of 33 m bounded by stably stratified layer below, which corresponds to a temperature gradient of $0.01 \text{ }^\circ\text{C m}^{-1}$. This initial mixed layer is much deeper than the decay depth of Stokes drift, thereby stabilizing wave-induced stratification, so that the effects of stabilizing wave-induced stratification and the stable stratification below the mixed layer are clearly separated. No surface wind stress is applied, and the Coriolis parameter is set to zero.

The computational domain is $256 \text{ m} \times 256 \text{ m} \times 96 \text{ m}$, evenly discretized into 256^3 grid boxes. This corresponds to a uniform grid spacing of $1 \text{ m} \times 1 \text{ m} \times 0.375 \text{ m}$. Doubly periodic boundary condition is used in the horizontal directions. A sponge layer that brings velocity and buoyancy to their initial values is used near the bottom in Oceananigans (Wagner et al. 2021). Radiation bottom boundary condition is used in NCAR LES (McWilliams et al. 1997). Both serve to avoid reflections of internal waves at the bottom of the domain. While all simulations are run for 48 hours to assess the robustness of turbulent statistics, we focus on the first 24 hours for analysis, during which robust horizontally averaged turbulent statistics can be collected by an additional temporal average over 12 hours from the model output (saved every 30 s) for most variables of interest (see more discussion on this in Section 4b). This also minimizes the impact of spurious TKE production induced by the turbulence-induced anti-Stokes flow (Pearson 2018), which accumulates over time.

238 **4. Stabilizing Effects by Opposing Eulerian Shear and Stokes Drift Shear in Oceananigans**

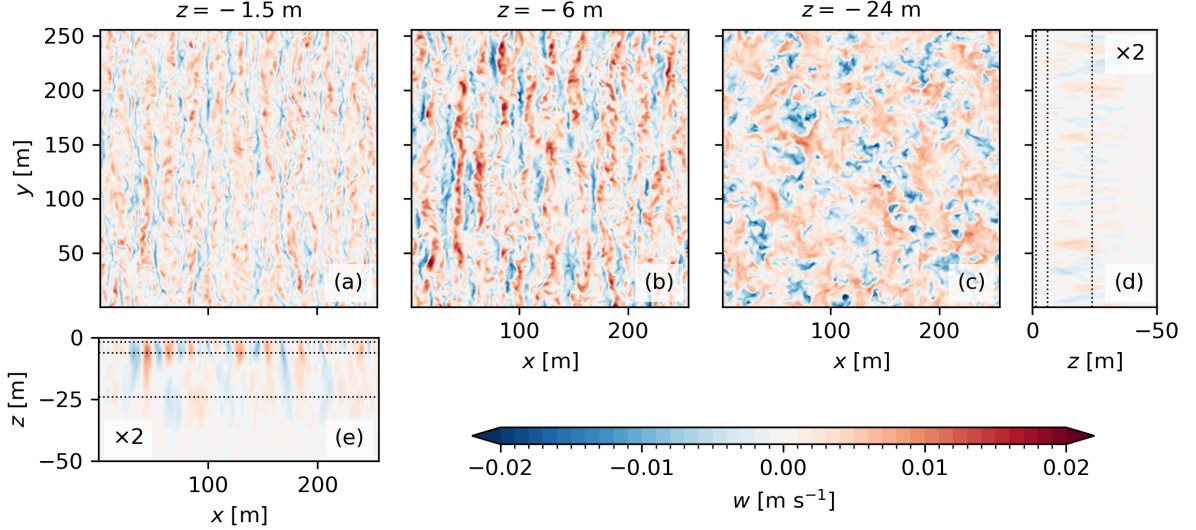
239 *a. Turbulence Structure*

240 Figure 1 shows the turbulence structure indicated by the vertical velocity snapshots at different
241 depths in the baseline case (“moderate-wave” with $Q_0 = 50 \text{ W m}^{-2}$). The roll structures with
242 alternating bands of upwelling and downwelling regions are clearly seen near the surface (roughly
243 upper 10 m). However, well below the surface, the turbulence structure resembles that of convective
244 turbulence, characterized by intense downwelling plumes. These roll structures near the surface are
245 very coherent, so that they can be clearly seen in the averaged vertical velocity along the crosswise
246 (y) direction (panel e). The fact that the near-surface vertical velocity averages to nearly zero in
247 the streamwise (x) direction supports the observation that these roll structures are aligned in the
248 crosswise direction. Below about 10 meters to the bottom of the boundary layer (around $z = 40 \text{ m}$),
249 structures of convective plumes can be seen in both streamwise and crosswise averages without a
250 directional preference.

257 The coherence of the roll structures depends on the relative importance of surface cooling and
258 wave forcing. Figure 2 compares the near-surface turbulence structure indicated by the vertical
259 velocity at $z = -1.5 \text{ m}$ among cases with different combinations of surface cooling and wave
260 forcing. There is a clear competition between the destabilizing surface cooling, which does not
261 have a preference in directions, and the stabilizing wave-induced stratification, which favors roll
262 structures in the crosswise direction. With stronger surface cooling and weaker wave forcing
263 (towards the lower left), the turbulence structure shows characteristics of convective plumes, with
264 weak upwelling regions enclosed by narrow and strong downwelling regions. These convective
265 cells are isotropic in streamwise and crosswise directions. As wave forcing becomes stronger
266 and/or surface cooling becomes weaker (towards the upper right), the narrow downwelling regions
267 start to align in the crosswise direction. And with sufficiently strong wave forcing or sufficiently
268 weak surface cooling, crosswise bands of upwelling and downwelling emerge.

273 *b. Turbulence Statistics*

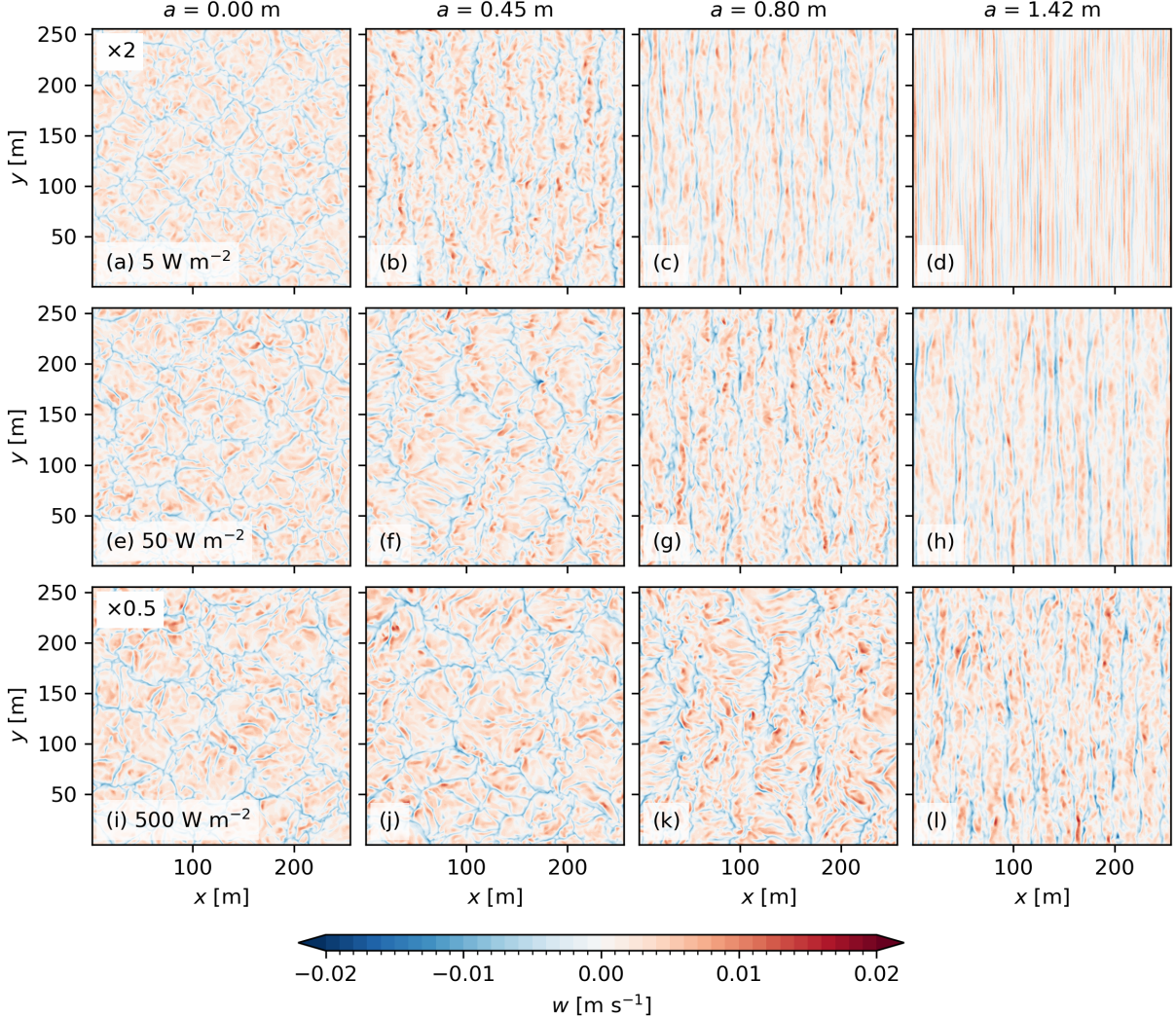
274 The horizontally and temporally averaged profiles of the mean fields and various turbulence
275 statistics are shown in Figure 3 for the four cases with moderate surface cooling of $Q_0 = 50 \text{ W m}^{-2}$.
276 Since there is no wind forcing at the surface, the vertical momentum fluxes are small and highly



251 FIG. 1. Snapshots of vertical velocity at $t = 24$ hr and a depth of (a) -1.5 m, (b) -6 m, and (c) -24 m for the
 252 baseline case with $Q_0 = 50 \text{ W m}^{-2}$ surface cooling and wave forcing with a wave amplitude of $a = 0.8 \text{ m}$. The
 253 streamwise (along x -direction) and crosswise (along y -direction) averaged vertical velocities are shown in panels
 254 (d) and (e), respectively. Dotted lines mark the depths at which the snapshots in panels (a)-(c) were taken. The
 255 values of the averaged vertical velocity are multiplied by a factor of 2 so that their structures can be clearly seen
 256 using the same colorbar.

277 variable due to the intermittency of convective plumes. Unlike other turbulence statistics, a 12-hour
 278 (or even 24-hour) average is not sufficient to generate a robust picture. Therefore, we plot the time
 279 evolution of horizontally averaged vertical momentum fluxes in Figure 4.

291 Although the simulations start from zero Lagrangian velocity, a turbulence-induced anti-Stokes
 292 flow (Pearson 2018) develops due to the anisotropy between $\overline{w'^2}$ and $\overline{u'^2}$ (Figure 3d,e), causing a net
 293 contribution of shear production and Stokes production in the $\overline{w'u'}$ budget. As a result, unlike pure
 294 convection in the “no-wave” case, the mean vertical turbulent flux of the streamwise momentum
 295 $\overline{w'u'}$ is nonzero. In the “strong-wave” case, for example, there is a net downward streamwise
 296 momentum transport $\overline{w'u'} < 0$ (Figure 4d), resulting in a negative Lagrangian flow near the surface
 297 (above $z \approx -5$ m) and a positive Lagrangian flow below (between $z \approx -20$ m and $z \approx -5$ m, red
 298 line in Figure 3a). No such effect is observed for $\overline{w'v'}$ in the crosswise direction (Figure 4h), and
 299 compared to weaker wave cases, $\overline{w'v'}$ is much less variable. Note that the turbulence-induced



269 FIG. 2. Snapshots of vertical velocity at $z = -1.5$ m and $t = 24$ hr under different combinations of surface
 270 cooling ($Q_0 = [5, 50, 500]$ W m^{-2} in the top, middle, and bottom rows) and wave conditions (wave amplitude
 271 $a = [0, 0.45, 0.8, 1.42]$ m in the four columns). Note that the vertical velocity in the cases with $Q_0 = 5 \text{ W m}^{-2}$
 272 and $Q_0 = 500 \text{ W m}^{-2}$ are multiplied by 2 and 0.5, respectively, to highlight the turbulence structure.

300 anti-Stokes flow is smaller than the Stokes drift, so the Eulerian flow is still opposing the Stokes
 301 drift, causing a stabilizing wave-induced stratification (Figure 3b).

302 Interestingly, substantially unstable stratification ($N^2 < 0$) is observed in the near-surface layer,
 303 where wave-induced stratification is strong so that the effective stratification $N_*^2 = N^2 - \partial_z \bar{u} \partial_z u^S$ is
 304 positive. This demonstrates the stabilizing effects induced by opposing Eulerian shear and Stokes

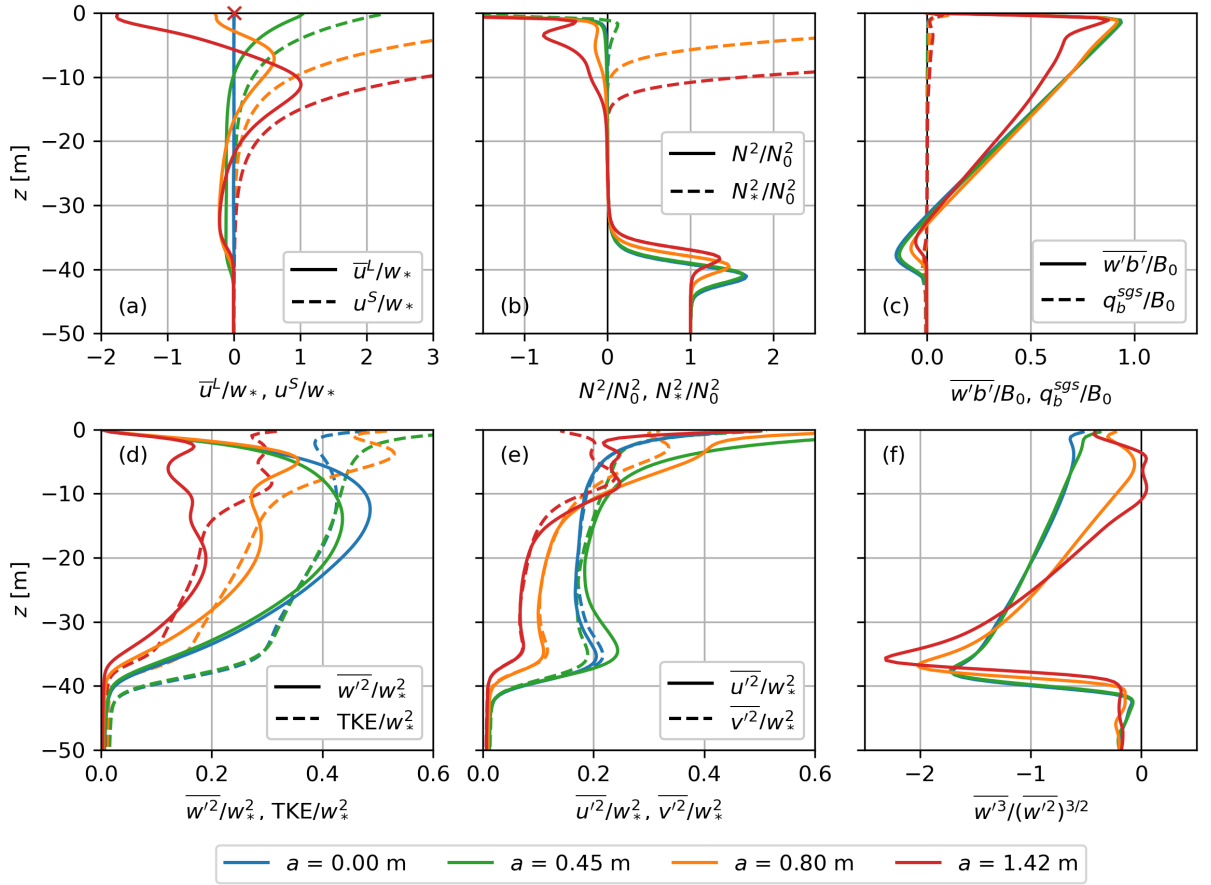
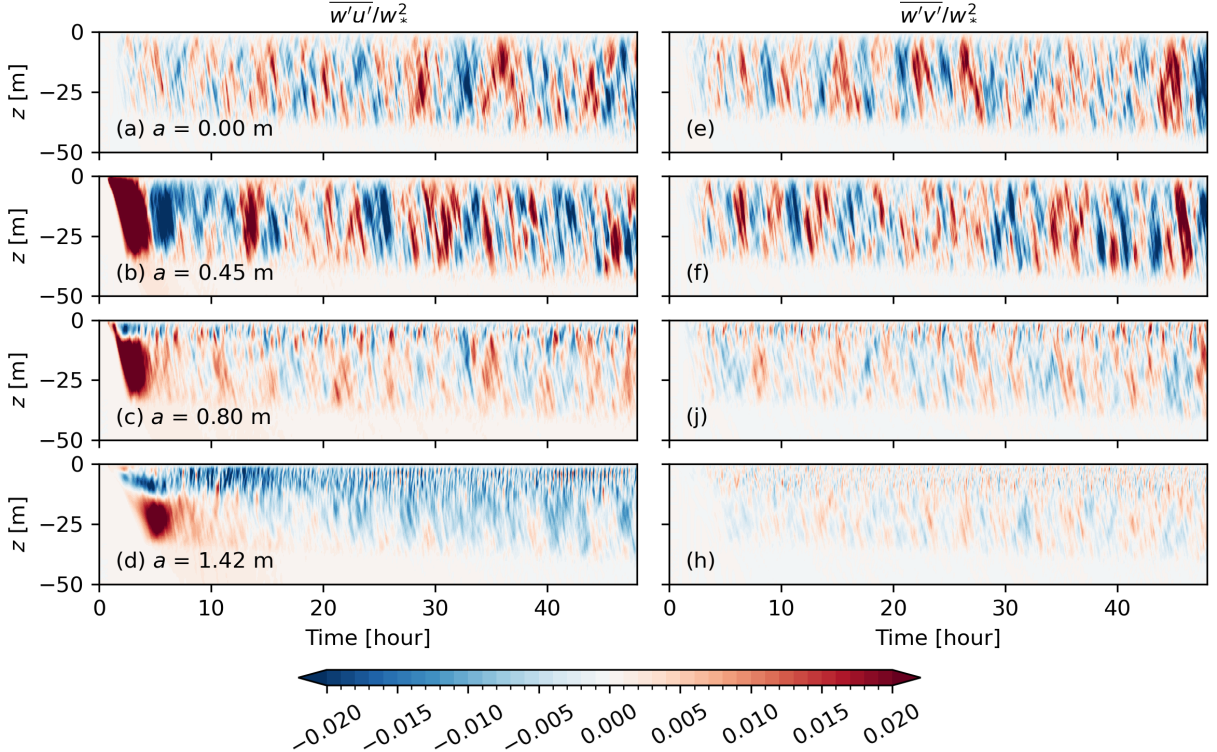


FIG. 3. Horizontally and temporally averaged profiles of normalized (a) streamwise Lagrangian velocity \bar{u} (solid) and Stokes drift u^S (dashed), (b) stratification N^2 (solid) and effective stratification $N_*^2 = N^2 - \partial_z \bar{u} \partial_z u^S$ (dashed), (c) resolved (solid) and SGS (dashed) vertical buoyancy flux $\bar{w}'b'$, (d) vertical velocity variance \bar{w}'^2 (solid) and TKE (dashed), (e) horizontal velocity variance \bar{u}'^2 (solid) and \bar{v}'^2 (dashed), and (f) the skewness of vertical velocity $\bar{w}'^3 / (\bar{w}'^2)^{3/2}$, for the cases with $Q_0 = 50 \text{ W m}^{-2}$. The surface buoyancy flux B_0 , convective velocity scale $w_* = (B_0 h_0)^{1/3}$ where h_0 is the initial mixed layer thickness, and initial stratification below the mixed layer N_0 are used in the normalization. The cross sign (\times) in (a) marks the vertically averaged Lagrangian velocity over the upper 50 m. Different colors show the results of simulations with different wave amplitude $a = [0.00, 0.45, 0.80, 1.42] \text{ m}$ in blue, green, orange, and red, respectively.

drift shear. Without such effect, convection rapidly develops and mixes the water column, bringing stratification close to neutral (blue line in Figure 3b). The effective stratification N_*^2 seems to be a useful indicator of stability in the water column in this case. In many ways, this is reminiscent



289 FIG. 4. Time evolution of vertical turbulent fluxes for (a-d) the streamwise momentum $\overline{w'u'}$ and (e-h) crosswise
 290 momentum $\overline{w'v'}$ for the cases with $Q_0 = 50 \text{ W m}^{-2}$.

308 of salt fingers in double diffusion (Leibovich 1983), where unstable buoyancy stratification due
 309 to surface cooling here acts as the salt gradient and stable wave-induced stratification acts as
 310 the temperature gradient. While the analogy to double diffusion in the “diffusive” regime has
 311 been fairly investigated in the context of two-dimensional Langmuir circulation in stable buoyancy
 312 stratification (e.g., Leibovich et al. 1989; Cox and Leibovich 1994), such an analogy in the “finger”
 313 regime has not been sufficiently explored (to the author’s knowledge).

314 With progressively stronger wave forcing, that is, progressively stronger wave-induced stable
 315 stratification, the vertical velocity variance becomes progressively weaker (Figure 3d). However,
 316 the horizontal velocity variance and, thereby, the TKE show more complex responses with mod-
 317 ified vertical structures. Near the surface where wave-induced stratification is strong, both the
 318 “moderate-wave” and “weak-wave” cases show a stronger horizontal velocity variance than the
 319 “no-wave” case (Figure 3e). Unlike in the “no-wave” case, anisotropy with $\overline{u'^2} > \overline{v'^2}$ is also ob-

served. The “strong-wave” case shows somewhat comparable horizontal velocity variance as the “no-wave” case and less anisotropy than the cases with weaker waves.

Below $z \approx -15$ m, the horizontal velocity variance in the “moderate-wave” and “strong-wave” cases is much weaker than in the “no-wave” case, while the isotropy between the two components is maintained ($\overline{u'^2} \approx \overline{v'^2}$). This may be due to the stabilizing effect of wave-induced stratification which weakens the connection between the surface cooling and the lower mixed layer, effectively dividing the mixed layer into two layers that are dominated by different dynamics. In the “weak-wave” case, the anisotropy between $\overline{u'^2}$ and $\overline{v'^2}$ persists throughout the mixed layer and $\overline{u'^2}$ is stronger than in the “no-wave” case. This is probably because wave-induced stratification is too weak to significantly weaken the downwelling convective plumes, through which the enhanced $\overline{u'^2}$ in the near-surface layer affects the lower layer. Consistently, the momentum fluxes are indeed most variable in the “weak-wave” case, as shown in Figure 4. In the “moderate-wave” and “strong-wave” cases, both $\overline{w'u'}$ and $\overline{w'v'}$ vary differently in the near-surface layer (above $z \approx -10$ m) and the layer below.

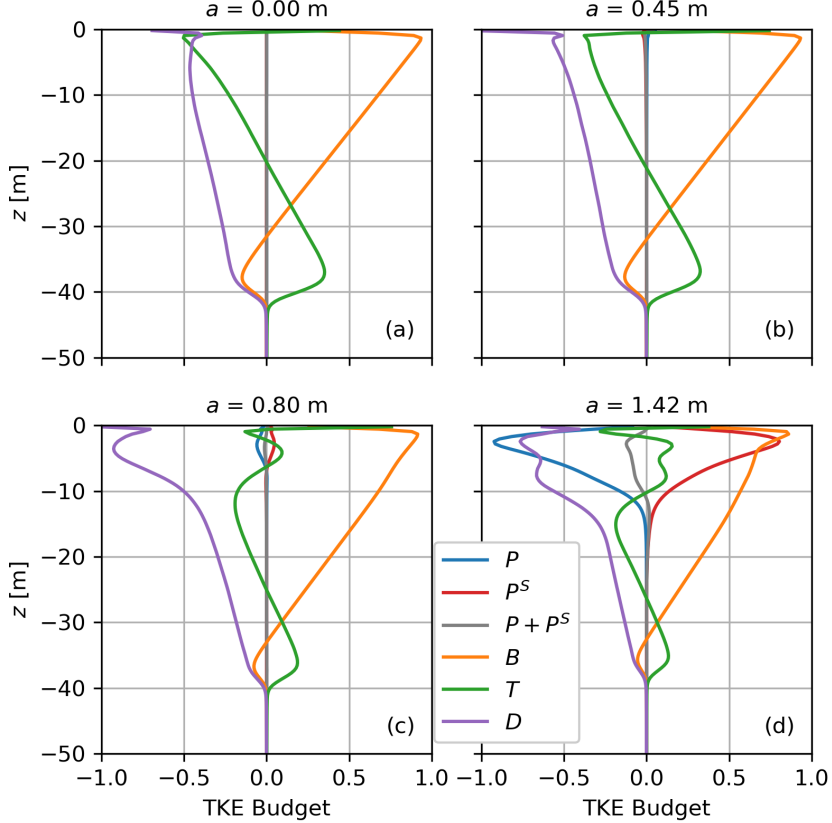
This two-layer structure is also reflected in the skewness of the vertical velocity (Figure 3f). The skewness of vertical velocity in both the “moderate-wave” and “strong-wave” cases are close to zero in the near-surface layer (due to the roll structures in Figure 1a,b) and return to being negative below (consistent with structures resembling convective plumes in Figure 1c). This is different from convective turbulence and Langmuir turbulence, both of which have stronger downwelling motions than upwelling motions near the surface, and thus negative skewness of vertical velocity.

c. Turbulent Kinetic Energy Budget

The stabilizing effects induced by opposing Eulerian shear and Stokes drift shear can also be seen in the TKE budget. The budget equation for the TKE, defined as $e = \frac{1}{2}|\mathbf{u}'|^2$, is (e.g., McWilliams et al. 1997),

$$\partial_t e = \underbrace{-\overline{w'\mathbf{u}'_h \cdot \partial_z \bar{\mathbf{u}}_h}}_P - \underbrace{\overline{w'\mathbf{u}'_h \cdot \partial_z \mathbf{u}^S}}_{PS} + \underbrace{\overline{w'b'}}_B - \underbrace{\partial_z \overline{w'p'}}_T - \underbrace{\partial_z \overline{w'e}}_D - \varepsilon, \quad (13)$$

where $\mathbf{u}_h = [u, v]$ is the horizontal component of the velocity. The terms on the right-hand side are shear production (P), Stokes production (PS), buoyancy production (B), pressure correlation and TKE transport terms (T), and dissipation (D).



347 FIG. 5. Horizontally and temporally averaged TKE budget terms normalized by the surface buoyancy flux for
 348 the cases with $Q_0 = 50 \text{ W m}^{-2}$.

349 Figure 5 shows the mean TKE budget terms for the four cases with $Q_0 = 50 \text{ W m}^{-2}$. In the
 350 “no-wave” case (panel a), the dominant balance is between buoyancy production, TKE transport,
 351 and dissipation, typical for convective turbulence. The TKE budget terms for the “weak-wave”
 352 case (panel b) is similar to the “no-wave” case with slightly stronger dissipation and weaker TKE
 353 transport near the surface. In the “moderate-wave” case (panel c), as the turbulence is more
 354 confined near the surface due to stabilizing wave-induced stratification, dissipation near the surface
 355 is stronger than the “no-wave” case. Buoyancy production near the surface is slightly modified by
 356 the change in the stratification (Figure 3b), but its contribution to the entrainment at the base of
 357 the mixed layer is much reduced. Given the largely counteracting Eulerian shear and Stokes drift
 358 shear, the net shear production is small. The dominant balance near the surface (above $z \approx -5 \text{ m}$) is
 359 between buoyancy production and dissipation. Stabilizing wave-induced stratification inhibits the

360 downward transport of TKE. As a result, the entrainment buoyancy flux at the base of the mixed
361 layer ($z \approx -40$ m) is also strongly reduced. Below $z \approx -5$ m, the TKE budget terms have structures
362 similar to the “no-wave” case, but smaller magnitude.

363 For the “strong-wave” case (panel d), stabilizing wave-induced stratification is so strong that it
364 significantly affects the vertical distribution of buoyancy production. In particular, it strongly mod-
365 ifies stratification and inhibits buoyancy production between $z \approx -10$ m and $z \approx -2$ m (Figure 3b,c).
366 Dissipation is still more confined to the surface. The downward momentum flux (Figure 3f) causes
367 a negative Lagrangian flow near the surface (above $z \approx -6$ m, Figure 3a) and positive Lagrangian
368 flow below, with a negative Lagrangian shear $\partial_z \bar{u}^L < 0$ above $z \approx -10$ m. This contributes to a
369 larger shear destruction than Stokes production (blue versus red in panel c). The TKE transport
370 term becomes a TKE source between $z \approx -10$ m and $z \approx -2$ m. Below $z \approx -15$ m, the TKE budget
371 is similar to the “moderate-wave” case but with even smaller magnitude.

372 5. An Alternative Solution?

373 a. NCAR LES vs. Oceananigans

374 We repeat the same experiments using NCAR LES and compare the results with those in
375 Oceananigans as presented in the previous section. Figures 6–8 show the same analyses for the
376 NCAR LES results. In the “no-wave” case, the results of NCAR LES are consistent with those of
377 Oceananigans, as expected (also see Section 2.5 of Fan et al. 2024). Similar results are also found
378 for the “weak-wave” case. However, interesting differences emerge when the effects of waves are
379 stronger.

380 In the “moderate-wave” case, rather than showing roll structures aligned in the crosswise direction
381 (perpendicular to the Stokes drift) as in Figure 1, the upwelling and downwelling streaks are
382 roughly aligned in the streamwise direction (parallel to the Stokes drift) in NCAR LES (Figure 6c).
383 These structures are reminiscent of parallel vortex tubes tilted and distorted by Stokes drift that
384 characterize Langmuir turbulence (Teixeira 2011), and are inconsistent with the most unstable
385 structure due to surface cooling in the presence of stabilizing wave-induced stratification, as
386 predicted by the linear stability analysis in Section 2.

387 Closer inspection in Figure 7 shows that the mean velocity profile in NCAR LES is signifi-
388 cantly different from Ocananaigans in the “moderate-wave” case. A strong vertical shear in the

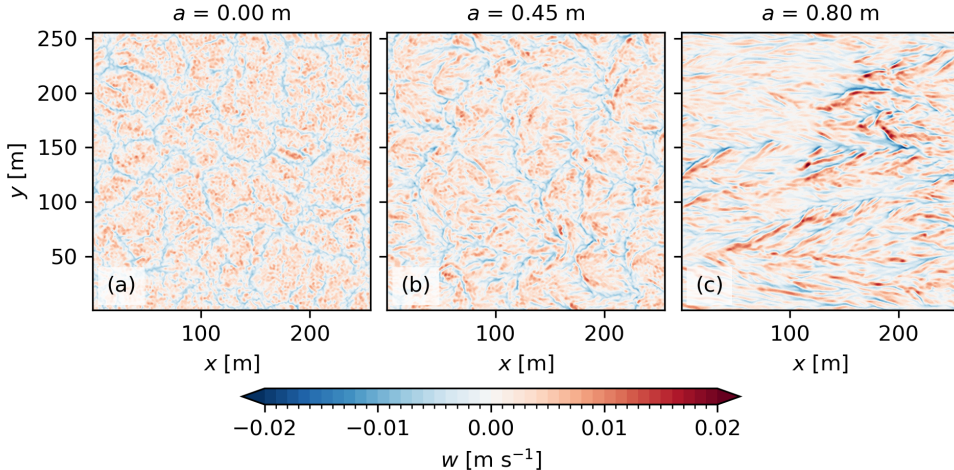
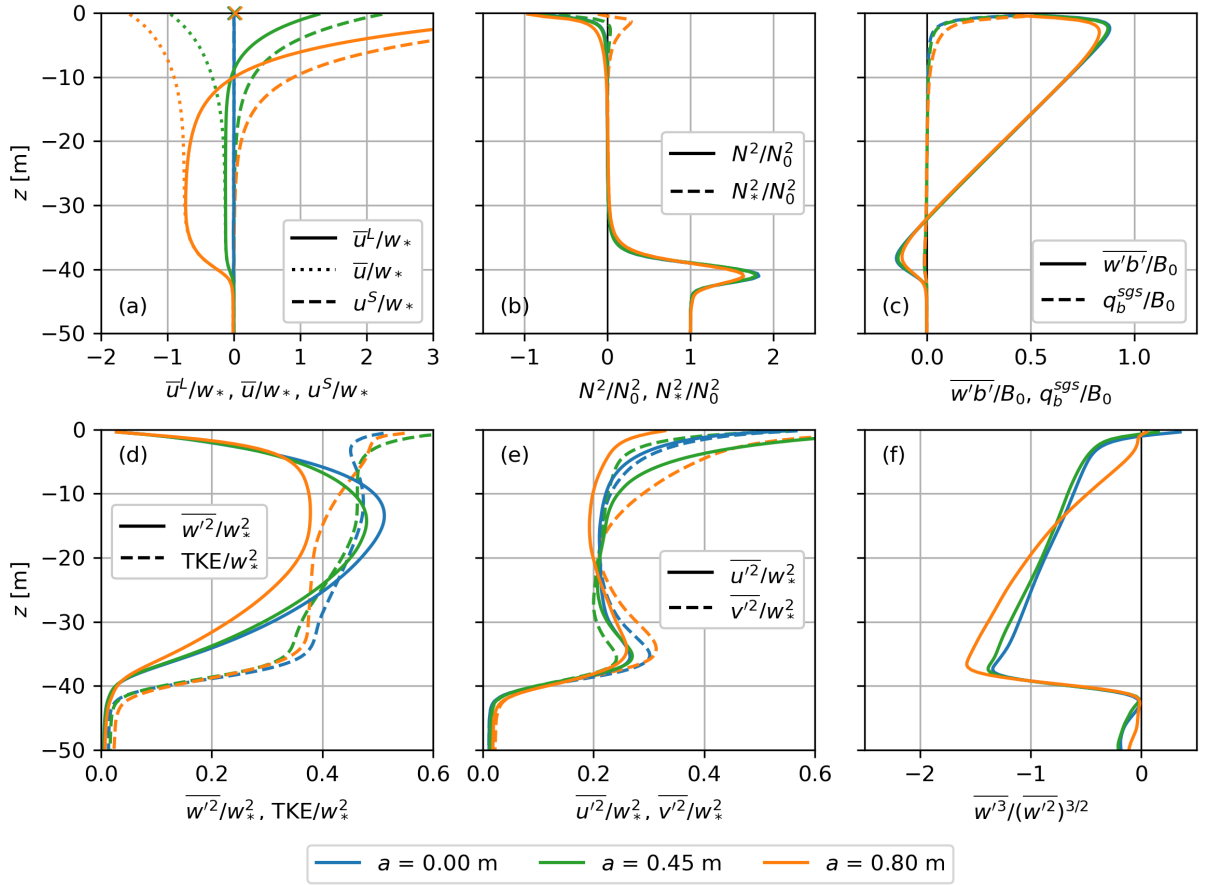


FIG. 6. Same as Fig. 2, but for NCAR LES with $a = [0, 0.45, 0.8]$ m and $Q = 50 \text{ W m}^{-2}$.

Lagrangian velocity is developed at the surface in the same direction as Stokes drift shear (panel a). Although starting with an initial Eulerian current that exactly cancels out the Stokes drift, such a stabilizing condition seems to be quickly weakened in NCAR LES, resulting in much weaker effective stratification N_*^2 (panel b) than in Oceananigans (Figure 3b). As a result, the weakening effect on the intensity of turbulence is also much smaller in NCAR LES than in Oceananigans, indicated by the smaller reduction in $\overline{w'^2}$ and TKE compared to the “no-wave” case (panel d). The anisotropy near the surface is reversed, being $\overline{u'^2} < \overline{v'^2}$ (panel e) rather than $\overline{u'^2} > \overline{v'^2}$ in Oceananigans (Figure 3e), consistent with the differences in the vertical velocity patterns (Figure 6c vs. Figure 1a). The skewness of the vertical velocity is also reduced near the surface (panel f), but to a lesser extent than in Oceananigans (Figure 3f).

Since the Eulerian shear is much weakened, the Eulerian shear production of TKE is small compared to the Stokes production (Figure 8b). The dissipation of TKE near the surface is also enhanced compared to the “no-wave” case in NCAR LES as a result of the intensified turbulence due to Stokes production, but is not as strongly confined to the surface as in Oceananigans. Unlike in Oceananigans, TKE transport is a net sink near the surface (similar to the “no-wave” case), suggesting an imbalance between TKE production (primarily buoyancy production) and dissipation. In addition, the reduction in TKE transport due to stabilizing wave-induced stratification (comparing the “moderate-wave” case with the “no-wave” case) is much weaker in NCAR LES.



407 FIG. 7. Same as Fig. 3, but for NCAR LES with $a = [0, 0.45, 0.8]$ m. The Eulerian velocity \bar{u} is also shown in
408 panel (a) by dotted lines.

409 Note that we have excluded the “strong-wave” case in the presentation of the NCAR LES results
410 here because the results in that case appear to be somewhat erroneous, with large variations in the
411 turbulent momentum fluxes that extend below the mixed layer and strong intermittency in other
412 turbulence statistics. Therefore, it is hard to get a robust picture of turbulence statistics in the
413 “strong-wave” case at this moment. Some level of intermittency is also seen in the “moderate-
414 wave” case, but much smaller. This issue seems to be stronger when the surface cooling is stronger,
415 so that the “strong-wave” case with $Q_0 = 500 \text{ W m}^{-2}$ cooling crashes after about 11 simulated
416 hours. This shows that NCAR LES may have some difficulty handling such extreme conditions.
417 An investigation of this behavior of NCAR LES is beyond the scope of this paper and left for future
418 studies.

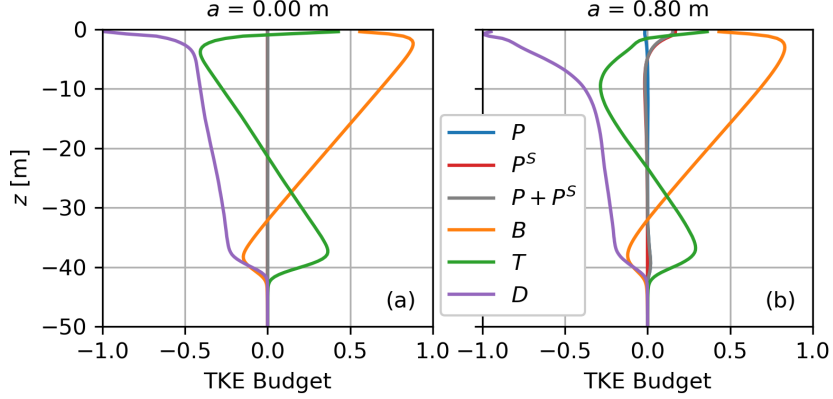
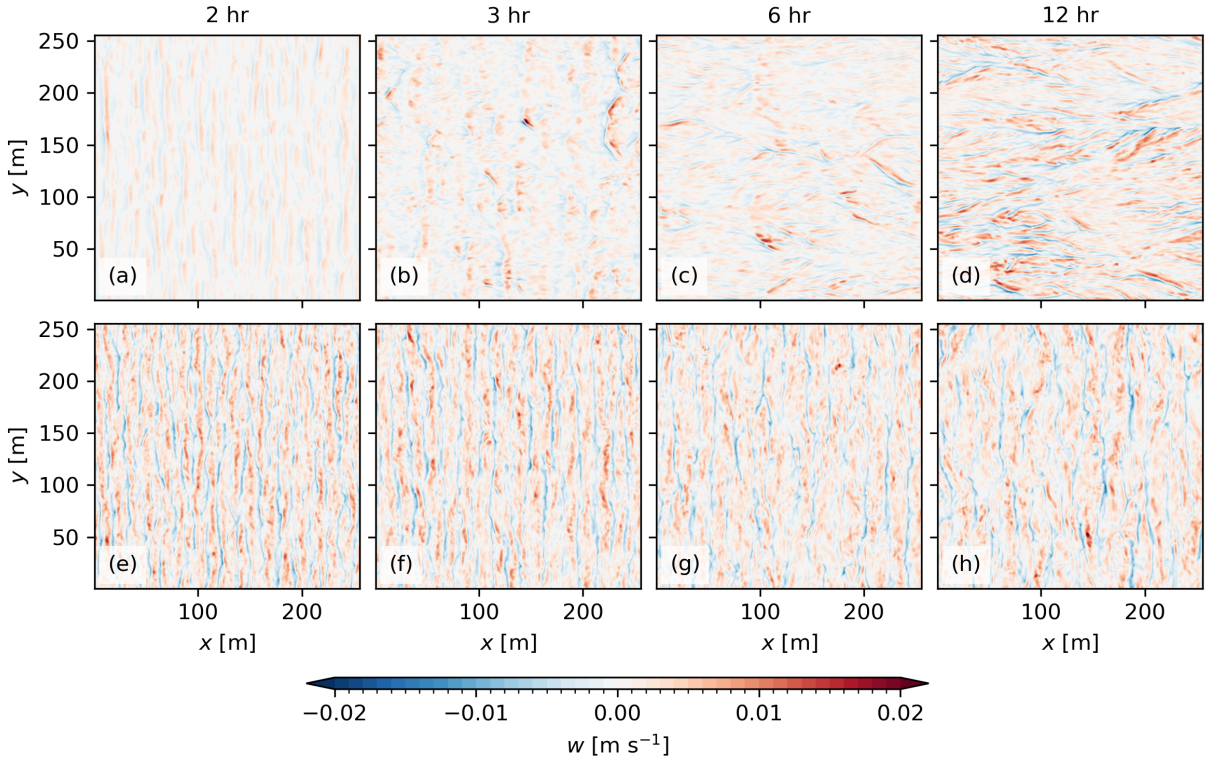


FIG. 8. Same as Fig. 5, but for NCAR LES with $a = [0, 0.8]$ m.

⁴¹⁹ *b. Time Evolution of the NCAR LES Solution*

⁴²⁰ The fact that NCAR LES and Oceananigans generate very different solutions in this simple
⁴²¹ idealized case is disturbing. The immediate question is, of course, why? But before diving into the
⁴²² details of the differences between the two LES models, it is helpful to note that both simulations
⁴²³ start from the same initial condition of zero Lagrangian flow. That is, initially, the stabilizing
⁴²⁴ effects induced by opposing Eulerian shear and Stokes drift shear should be the same between
⁴²⁵ the two LES models. While this initial condition is largely maintained under zero wind stress in
⁴²⁶ Oceananigans to the extent of changes due to turbulence-induced anti-Stokes drift (Pearson 2018),
⁴²⁷ significant changes in Eulerian velocity are seen in NCAR LES. The near-surface Eulerian shear is
⁴²⁸ much reduced in NCAR LES in a quasi-equilibrium state, resulting in much weaker wave-induced
⁴²⁹ stratification. It seems that the differences in the turbulence structure and statistics between the two
⁴³⁰ LES models are rooted in the different simulated velocity profiles. To show this, we take a closer
⁴³¹ look at the time evolution of the NCAR LES solution.

⁴³² Figure 9a–d shows the vertical velocity snapshots at four different time instants for the “moderate-
⁴³³ wave” case with $Q_0 = 50 \text{ W m}^{-2}$ in NCAR LES. Indeed, the roll structures aligned in the crosswise
⁴³⁴ direction are seen in NCAR LES at early stages of the simulation (panels a, b). Only after a few
⁴³⁵ hours do the roll structures get distorted and evolve in the streamwise direction. The time evolution
⁴³⁶ of the velocity profiles in Figure 10a confirms that the differences in the turbulent structures are
⁴³⁷ the result of differences in the mean velocity shear. In the early stages of the simulation (around
⁴³⁸ $t = 2 \text{ hr}$), the near-surface Eulerian velocity shear is still strong and comparable to the Stokes drift

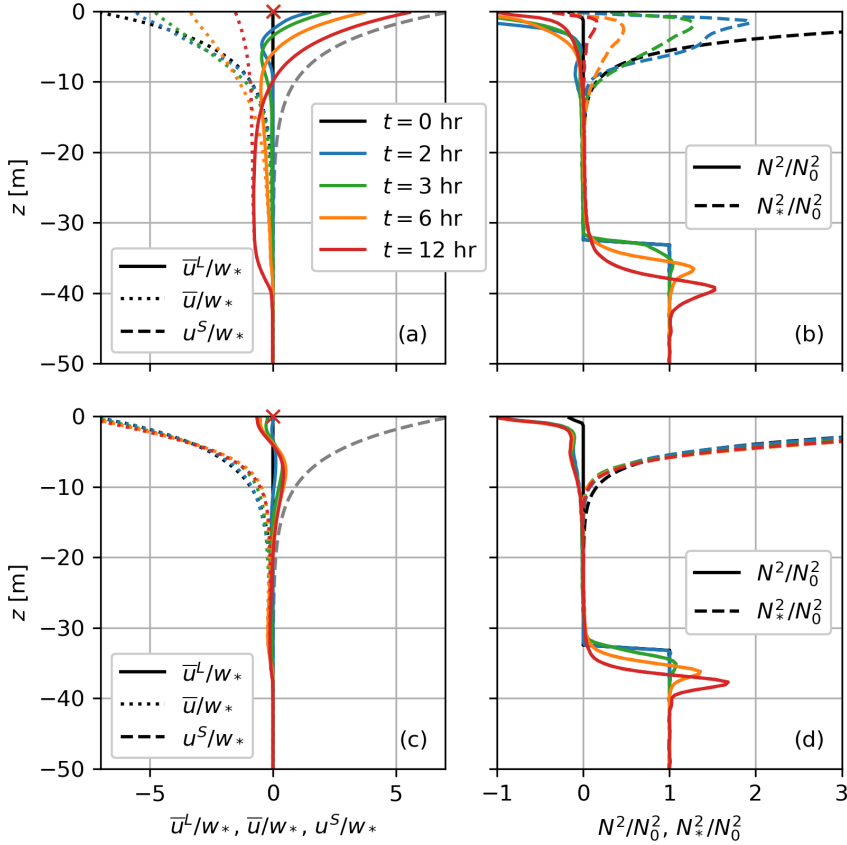


445 FIG. 9. Snapshots of vertical velocity at four different time instants (at $t = [2, 3, 6, 12]$ hr) for the “moderate-
 446 wave” case with $Q_0 = 50 \text{ W m}^{-2}$ in NCAR LES. Panels (a)–(d) show the time evolution in the run with
 447 down-Eulerian shear mixing assumption in the SGS model, and panels (e)–(h) show the results with down-
 448 Lagrangian shear mixing assumption.

439 shear. The condition of opposing Eulerian shear and Stokes drift shear $\partial_z \bar{u} = -\partial_z u^S$ still holds
 440 to a sufficient degree so that the linear instability analysis in Section 2 applies. However, as the
 441 near-surface Eulerian velocity shear gradually decreases and the resulting effective stratification
 442 weakens, the turbulence structures are increasingly being affected by the tilting and stretching
 443 effects of Stokes drift shear (Teixeira 2011). Now the question becomes, why does the simulated
 444 mean velocity behave so differently in NCAR LES and Oceananigans?

456 c. Down-Eulerian Shear Mixing or Down-Lagrangian Shear Mixing?

457 A key difference between NCAR LES and Oceananigans is the different assumptions adopted by
 458 their SGS models, specifically, down-Eulerian shear mixing in NCAR LES and down-Lagrangian
 459 shear mixing in Oceananigans. These assumptions are natural choices for solving the CL equation



449 FIG. 10. Horizontally averaged profiles of normalized (a,c) streamwise Lagrangian velocity \bar{u}^L (solid),
 450 Eulerian velocity \bar{u} (dotted), and Stokes drift u^S (dashed), (b,d) stratification N^2 (solid) and effective stratification
 451 $N_*^2 = N^2 - \partial_z \bar{u} \partial_z u^S$ (dashed), taken at four different time instants (at $t = [2, 3, 6, 12]$ hr) for the “moderate-wave”
 452 case with $Q_0 = 50 \text{ W m}^{-2}$ in NCAR LES. The cross sign (\times) in (a) and (c) marks the vertically averaged Lagrangian
 453 velocity over the upper 50 m. Panels (a) and (b) show the time evolution in the run with down-Eulerian shear
 454 mixing assumption in the SGS model, and panels (c) and (d) show the results with down-Lagrangian shear
 455 mixing assumption.

460 in the Eulerian form (11) and the Lagrangian form (10), respectively. It is often assumed that
 461 an SGS model should play a minimal role in the solution of an LES. However, in this idealized
 462 case, it matters by affecting how the boundary conditions are applied to the resolved flows in
 463 the LES. Since there is no Stokes drift in the crosswise direction and thus no difference between
 464 Eulerian and Lagrangian flows, we can restrict our discussion in the streamwise direction only.
 465 A boundary condition of zero wind stress ($\tau_x^0 = 0$) translates into a boundary condition of zero

mean Eulerian shear ($\partial_z \bar{u}|_{z=0} = 0$) in NCAR LES since $0 = \tau_x^0 = \bar{\tau}_{xz}^{sgs}|_{z=0} \sim -\bar{\nu}_{sgs} \partial_z \bar{u}|_{z=0}$ under horizontal homogeneous conditions, where τ_{xz}^{sgs} is the xz component of the SGS stress tensor and ν_{sgs} is the SGS turbulent viscosity. In contrast, it translates into a boundary condition of zero mean Lagrangian shear ($\partial_z \bar{u}^L|_{z=0} = 0$) in Oceananigans ($0 = \tau_x^0 = \bar{\tau}_{xz}^{sgs}|_{z=0} \sim -\bar{\nu}_{sgs} \partial_z \bar{u}^L|_{z=0}$). Starting from zero Lagrangian flow, the initial condition is consistent with the boundary condition in Oceananigans. Therefore, the initial condition of a zero Lagrangian flow is largely maintained in the simulation without any external forces, except the development of a small turbulence-induced anti-Stokes flow (Pearson 2018). However, there is a mismatch between the initial condition of zero Lagrangian flow (which implies $\partial_z \bar{u} = -\partial_z u^S$) and the boundary condition of zero mean Eulerian shear ($\partial_z \bar{u}|_{z=0} = 0$) in NCAR LES. The Eulerian flow in NCAR LES therefore adjusts to the boundary condition and the initial Eulerian shear is gradually mixed away by convective turbulence while the depth-averaged Eulerian velocity is unchanged.

To demonstrate this, the SGS model in NCAR LES is modified to employ a down-Lagrangian shear mixing assumption. This is done by simply adding Stokes drift shear to the strain tensor when computing τ_{xz}^{sgs} while keeping ν_{sgs} unchanged. More careful treatment may be required to accurately incorporate down-Lagrangian shear mixing in NCAR LES, especially to include the effect of Lagrangian shear on ν_{sgs} . However, this simple modification is easy to implement and sufficiently serves our purpose in demonstrating the difference in assuming down-Lagrangian shear versus down-Eulerian shear mixing. The results are shown in Figures 9e–h and 10c,d. Indeed, with a down-Lagrangian shear mixing assumption in the SGS model in NCAR LES, the initial condition of zero Lagrangian flow is now largely maintained, and the solution becomes similar to that in Oceananigans.

6. Discussion

a. Evidence of Stabilizing Wave-Induced Stratification in the Literature

The scenario of exactly opposing Eulerian shear and Stokes drift shear described in this paper is highly idealized to demonstrate the stabilizing wave-induced stratification. In reality, Eulerian shear in a typical wind-driven ocean surface boundary layer often aligns well with the Stokes drift shear of locally generated wind waves, promoting the formation of Langmuir turbulence (e.g., Leibovich 1983; McWilliams et al. 1997). In addition, wave-following Eulerian shear can also be induced by

495 momentum transfer from waves to currents in the viscous boundary layer (Longuet-Higgins 1953),
496 which is similarly unstable by the CL mechanism (Craik 1982) and may further enhance Langmuir
497 turbulence as demonstrated in wave-resolving simulations (see, e.g., Tsai et al. 2017; Fujiwara
498 et al. 2020). However, stabilizing effects are present as long as there is a component of Eulerian
499 shear $\partial_z \bar{\mathbf{u}}_c$ opposing Stokes drift shear, such that $\partial_z \bar{\mathbf{u}}_c \cdot \partial_z \mathbf{u}^S < 0$ (Leibovich 1977, 1983), although
500 it may be hidden behind the scene if other forcings are dominant. This condition could be satisfied
501 when the wind and waves have a misalignment angle greater than 90° (Van Roekel et al. 2012;
502 Sullivan et al. 2012), in the presence of remotely generated swell waves (McWilliams et al. 2014;
503 Wagner et al. 2021), in frontal regions where a geostrophic along-front current is established by a
504 horizontal buoyancy gradient that is not necessarily aligned with the waves (Suzuki et al. 2016), or
505 in coastal regions where currents are strongly influenced by tides and topography (Kukulka et al.
506 2011; Shrestha et al. 2019).

507 For example, in the LESs of Langmuir turbulence influenced by swell waves as described in
508 McWilliams et al. (2014), the addition of a swell component of Stokes drift induces an anti-Stokes
509 Eulerian flow that opposes the Stokes drift due to planetary rotation (McWilliams and Restrepo
510 1999; Polton et al. 2005). The stabilizing effect induced by opposing Eulerian shear and Stokes drift
511 shear, as discussed here, should play a role in virtually all test cases in McWilliams et al. (2014),
512 although its manifestation depends on its competition with destabilizing Langmuir turbulence.
513 There are at least two test cases in which such stabilizing effect seems evident. One is their “weak
514 wind” case with a wind speed of $U_a = 2.5 \text{ m s}^{-1}$, which shows a decrease in normalized vertical
515 velocity variance with decreasing turbulent Langmuir number (blue dashed lines in their Figure 8)
516 and roll structures perpendicular to the swell component of Stokes drift (their Figure 12). The other
517 is their “northward swell” case, which has weaker normalized vertical velocity variance than the
518 “no swell” case (their Figure 7), and also shows roll structures perpendicular to the swell component
519 of Stokes drift below the surface (their Figure 11). Their “southward swell” case also shows a much
520 weaker vertical velocity variance but very different turbulence structure. This asymmetry may be
521 due to the difference in the total Lagrangian velocity in the swell direction (their Figure 3), which
522 is close to zero in the “northward swell” case (thus more similar to the idealized case discussed
523 here), but large in the “southward swell” case.

Another example can be found in the comparison of boundary layer turbulent mixing following rapid versus gradual surface wave growth in Wagner et al. (2021). Rapid and gradual surface wave growth are represented, respectively, by an “excited” initial condition with $\mathbf{u}^L|_{t=0} = \mathbf{u}^S$ and a “resting” initial condition with $\mathbf{u}^L|_{t=0} = 0$. In their Figures 7 and 8, Wagner et al. (2021) showed that an “excited” initial condition results in stronger turbulent mixing and thus more rapid deepening of the boundary layer than the “resting” initial condition in the early stages of the simulations. They attributed this difference in turbulence intensity to the stronger near-inertial shear generated by the “excited” initial condition. However, such a difference can also be seen in similar cases without rotation (not shown), and thus may not necessarily be explained by the development of near-inertial shear. Instead, these different responses to different initial conditions could probably be more easily understood from the perspective of stabilizing wave-induced stratification. A “resting” initial condition poses a stabilizing wave-induced stratification in the early stages of the simulation and reduces turbulent mixing, until the wind-driven shear reverses the sign of Eulerian shear. In contrast, an “excited” initial condition does not have such a stabilizing effect. Interestingly, Wagner et al. (2021) also found that coherent roll structures tend to align in the direction perpendicular to Stokes drift as the surface stress forcing dies out, the mean Lagrangian shear weakens, while Stokes drift remains unchanged (their Figure 5). This seems to be a situation similar to the idealized test case discussed here, where the stabilizing effect induced by opposing Eulerian shear and Stokes drift is dominant.

543 *b. Implications for Parameterizations*

The stabilizing effects induced by opposing Eulerian shear and Stokes drift shear have not yet been parameterized in most wave-driven mixing parameterizations, which have placed more emphasis on the destabilizing scenario with aligned Eulerian shear and Stokes drift shear that promotes Langmuir turbulence (Li et al. 2019). An exception is the second-moment closure model of Langmuir turbulence by Harcourt (2013), in which $\partial_z \bar{\mathbf{u}} \cdot \partial_z \mathbf{u}^S$ is explicitly considered and should be able to account for the scenario of opposing Eulerian shear and Stokes drift shear. However, the tuning of free parameters in this model is still based on LES in the condition of aligned wind and waves.

552 One implication of the idealized test case presented here in wave-driven mixing parameterizations
553 is that Eulerian shear and Stokes drift shear have vastly different influences on turbulent mixing and
554 therefore may not simply be combined into a Lagrangian shear, even though it could sometimes be
555 skillful (e.g., McWilliams et al. 2012). In extreme cases of perfectly opposing Eulerian shear and
556 Stokes drift shear, waves impose a stabilizing effect on turbulence whose strength depends on the
557 Stokes drift shear. This effect cannot be described by the Lagrangian shear alone, which is zero
558 in this case. At a minimum, the influence of Eulerian shear and Stokes drift shear on turbulence
559 should probably be considered separately in a parameterization (e.g., Harcourt 2013).

560 Wave-induced stratification may be a useful indicator when combined with buoyancy stratification
561 to describe the stability of the water column. In a sufficiently deep mixed layer, it effectively
562 separates the mixed layer into two, an upper layer in which the turbulence structures are strongly
563 modified, and a lower layer in which the turbulence structures are largely unchanged but the
564 turbulence intensity is much weakened. These two layers might need different treatments in
565 parameterizations. Incorporating the stabilizing effects induced by opposing Eulerian shear and
566 Stokes drift shear as described in this study in wave-driven mixing parameterizations, probably by
567 modifying the Monin-Obukhov similarity theory (e.g., Large et al. 2019), may be a promising path
568 forward. It could potentially help reduce errors of Langmuir turbulence parameterizations under
569 weak wind forcing or stable surface conditions as highlighted in the multi-model comparison by
570 Li et al. (2019).

571 *c. Analogy With Background Rotation*

572 It is clear from the Lagrangian formulation of the CL equation (10) that there is an analogy
573 between the Stokes drift term (the fifth term on the right-hand side) and the Coriolis force (the
574 fourth term on the right-hand side). Together, these two terms give a Lagrangian mean Coriolis
575 force, $-(\mathbf{f} - \nabla \times \mathbf{u}^S) \times \mathbf{u}^L$, where $\mathbf{f} - \nabla \times \mathbf{u}^S$ can be viewed as the effective background rotation felt by
576 the Lagrangian flow (Holm 1996; Teixeira 2011). For horizontally homogeneous Stokes drift that
577 decays with depth ($\mathbf{u}^S = [u^S(z), 0, 0]$) as considered in this study, the effective background rotation
578 due to Stokes drift ($-\nabla \times \mathbf{u}^S = [0, -\partial_z u^S, 0]$) only has a horizontal component. It is therefore
579 analogous to the horizontal component of Earth's rotation f_* in the non-traditional approximation
580 of the Coriolis force with $\mathbf{f} = [0, f_*, f]$. Such analogy is also discussed by Wagner and Constantinou

581 (2025), who explored many interesting features of decaying isotropic shear-free turbulence beneath
582 surface waves through an analogy with rotating turbulence, including the development of depth-
583 alternating jets (as also seen in Figure 3a) which is analogous to alternating jets in β -plane
584 turbulence.

585 Using this analogy, the idealized case discussed in this study is similar to the problem of
586 convection at the equator driven by surface cooling and without the influence of surface waves,
587 except that $\partial_z u^S$ varies with depth while f_* does not. Wang (2006) reported a small but noticeable
588 weakening of $\overline{w'^2}$ and a slight increase in the depth ranges with negative N^2 when f_* is considered in
589 their LES of oceanic convective turbulence at a latitude of 60°N (their Figure 1). This is consistent
590 with the results in Section 4. At the equator, f_* reaches its maximum of $\sim 1.45 \times 10^{-4} \text{ s}^{-1}$. For
591 the “moderate-wave” case discussed in this study, $\partial_z u^S$ has a maximum value of $2a^2 k^2 \sqrt{gk} \approx$
592 $1.42 \times 10^{-2} \text{ s}^{-1}$ at the surface, two orders of magnitude greater than $\max(f_*)$. Therefore, although
593 the effect of f_* on oceanic convection as shown in Wang (2006) is relatively small, the stabilizing
594 effect of opposing Eulerian shear and Stokes drift shear, as demonstrated here, could have a much
595 larger impact.

596 This analogy between Stokes drift and background rotation extends beyond the simple idealized
597 case discussed here, in particular in the presence of wind-driven shear. The horizontal component
598 of Earth’s rotation is shown to significantly affect the instability of the Ekman layer (e.g., Leibovich
599 and Lele 1985). It also leads to a dependence of ocean surface vertical mixing on the direction
600 of surface wind stress, with the weaker (stronger) vertical mixing driven by the westerly (easterly)
601 wind (e.g., Garwood et al. 1985). This dependence of vertical mixing on wind direction was nicely
602 demonstrated in a set of idealized LES by Liu et al. (2018). Similarly, the effect of Stokes drift can
603 be destabilizing or stabilizing depending on the sign of $\partial_z \bar{\mathbf{u}} \cdot \partial_z \mathbf{u}^S$ (Leibovich 1977, 1983). In the
604 destabilizing regime ($\partial_z \bar{\mathbf{u}} \cdot \partial_z \mathbf{u}^S > 0$), Langmuir turbulence emerges and its strength decreases with
605 increasing misalignment between the Stokes drift and surface wind (e.g., Van Roekel et al. 2012;
606 Sullivan et al. 2012; Wang et al. 2019). In the stabilizing regime ($\partial_z \bar{\mathbf{u}} \cdot \partial_z \mathbf{u}^S < 0$), one may also
607 expect that the strength of such a stabilizing effect depends on the misalignment angle. In addition,
608 wave-like solutions can be found in the stabilizing regime, which are analogous to near-inertial
609 waves. There is considerable existing literature on the effect of the horizontal component of Earth’s
610 rotation on near-inertial waves (e.g., Gerkema and Shrira 2005; Tort and Winters 2018), which can

611 serve as a useful guide to explore the potential effect of ocean surface waves on the evolution of
612 near-inertial waves in the upper ocean (also see Wagner et al. 2021).

613 *d. Does Sub-Grid Scale Model Matter?*

614 Although being extremely idealized, the test case described here proves to be useful in exposing
615 subtle differences between different LES models and limitations of solving the CL equation using
616 the LES technique. It is a case where the turbulence-induced anti-Stokes drift (Pearson 2018)
617 dominates the mean flow. Under no-wind condition, assuming down-Eulerian shear mixing and
618 down-Lagrangian shear mixing in the SGS model lead to completely different boundary conditions
619 for the mean flow. A zero wind stress translates to zero Eulerian shear at the surface when down-
620 Eulerian shear mixing is assumed, or zero Lagrangian shear when down-Lagrangian shear mixing
621 is assumed. This difference changes the vertical structure of the mean flow and results in different
622 turbulence structures and their anisotropy.

623 It is common practice to initialize an LES of Langmuir turbulence with an initial mixed layer
624 from zero Lagrangian velocity (e.g., Harcourt and D'Asaro 2008; Li and Fox-Kemper 2017). One
625 practical reason for this choice is to minimize the inertial oscillation generated by the sudden
626 onset of velocity at the beginning of the simulation (e.g., Wagner et al. 2021), which is not in
627 balance with surface forcing. The results here show that this initial condition of zero Lagrangian
628 velocity imposes a stabilizing wave-induced stratification on the water column and suppresses the
629 development of turbulence. In an LES that employs a down-Eulerian shear mixing assumption in
630 its SGS model, there is an initial mixing of the Eulerian velocity that quickly destroys the stabilizing
631 wave-induced stratification. However, if a down-Lagrangian shear mixing is assumed in the SGS
632 model, such stabilizing wave-induced stratification is maintained if there is no other external forcing
633 on the streamwise momentum. In typical Langmuir turbulence cases with substantial wind forcing
634 (Harcourt and D'Asaro 2008; Li and Fox-Kemper 2017), such differences should be relatively
635 small. But in weakly forced cases like the one here, such differences cannot be ignored and care
636 must be taken.

637 Although the down-Lagrangian shear mixing assumption is shown to be necessary to maintain
638 the initial zero Lagrangian velocity in this idealized case, whether it is more appropriate than
639 the down-Eulerian shear mixing assumption is still an active research question, which probably

has received less attention than it should have. Wagner et al. (2021) discussed this issue in their Appendix A and showed that a down-Lagrangian shear mixing assumption in the SGS model is necessary to guarantee a positive definite dissipation rate of the Lagrangian-mean kinetic energy $|\mathbf{u}^L|^2/2$ and thus a forward cascade of $|\mathbf{u}^L|^2/2$ across the filter scale. As shown in Holm (1996), the Lagrangian formulation of the CL equation in (10) has the advantage that the Stokes drift term $(\nabla \times \mathbf{u}^S) \times \mathbf{u}^L$ is perpendicular to \mathbf{u}^L and thus does no work on \mathbf{u}^L . Therefore, $|\mathbf{u}^L|^2/2$ is conserved in the absence of buoyancy, dissipation, and nonzero $\partial_t \mathbf{u}^S$, an appealing property when formulating the SGS model (Wagner et al. 2021). In contrast, the conservation of $|\mathbf{u}|^2/2$ derived from the Eulerian formulation of the CL equation (either (1) or (11)) requires consideration of the work done by the Stokes Coriolis force (see Section 2.4 of Suzuki and Fox-Kemper 2016). Since \mathbf{u}^S is prescribed in the CL equation, the conservations of $|\mathbf{u}^L|^2/2$ and $|\mathbf{u}|^2/2$ are ultimately linked. However, their physical interpretations are different, as they represent different mean properties of the flow. It is beyond the scope of this paper to answer the question of which SGS model is more appropriate. But the principle of forward cascade of kinetic energy across the filter scale in an LES (e.g., Wagner et al. 2021) is an important constraint for an SGS model. In practice, one difficulty in solving the CL equation using LES is due to the effect of Stokes drift on the anisotropy of turbulence (e.g., Li et al. 2005; Teixeira 2011; Li and Fox-Kemper 2020), which depends on $|\partial_z \mathbf{u}^S|$ and can be large at the surface even at the grid scale for typical configurations. Inadequate resolution of this effect may invalidate the assumption of a forward cascade of kinetic energy adopted in the SGS model. When such an effect is not fully resolved, something like the special treatment for the influence of near-surface mean shear in the two-part SGS model in Sullivan et al. (1994) may be useful to account for the effect of Stokes drift shear on SGS stresses separately. The need to include the effect of Stokes drift in the SGS model is also suggested by Pearson (2018). Explorations along these lines are left for future study.

7. Summary

The presence of surface gravity waves affects the stability of the water column in the ocean surface boundary layer according to the CL theory (Craik and Leibovich 1976; Leibovich 1977, 1983). In addition to causing instability and generating Langmuir turbulence when the Eulerian shear and Stokes drift shear are aligned (Leibovich 1983; Thorpe 2004; Sullivan and McWilliams

669 2010; D'Asaro 2014), it can also provide a stabilizing effect when the Eulerian shear and Stokes drift
670 shear are opposite, which acts effectively as a stabilizing wave-induced stratification (Leibovich
671 1983; Bühler 2014). Here, we demonstrate such stabilizing effect in LES using an idealized test
672 case with homogeneous surface cooling, no wind stress, and no rotation.

673 Under the combined influence of destabilizing surface cooling and stabilizing wave-induced
674 stratification, turbulence structures are significantly modified. When stabilizing wave-induced
675 stratification is strong, roll structures of convective motions form, and the resulting bands of
676 upwelling and downwelling regions are aligned in the crosswise direction perpendicular to Stokes
677 drift. This is vastly different from horizontally isotropic cell structures in convective turbulence and
678 pairs of streamwise vortical structures aligned with Stokes drift in Langmuir turbulence. Although
679 convective motions in the roll structures are still driven by surface cooling, their alignment is a result
680 of the directional preference of stabilizing wave-induced stratification, which selectively stabilizes
681 fluctuation in the crosswise direction. Interestingly, persistent negative buoyancy stratification is
682 seen when stabilizing wave-induced stratification is strong, suggesting a compensation between
683 the two. This could potentially be a useful indicator that evidences the presence of the stabilizing
684 wave-induced stratification in observations.

685 Using this idealized case, we show that the formulation of an SGS model, specifically whether
686 assuming down-Lagrangian shear mixing or down-Eulerian shear mixing, could potentially be
687 important influencing the mean flow and thus resolved turbulent structures in the LES. The down-
688 Lagrangian shear mixing is shown to be necessary to maintain the initial zero Lagrangian velocity in
689 this idealized case without surface wind forcing. However, solutions under such extreme conditions
690 may require validation against observations or laboratory experiments. Future work is needed to
691 address the questions of which formulation is more appropriate to solve the CL equation in LES or
692 if alternative formulations are necessary. Before that, great care should be taken when designing
693 and interpreting the LES that solves the CL equation with misaligned currents and waves.

694 *Acknowledgments.* This work benefited from many interesting discussions with Bicheng Chen,
695 Baylor Fox-Kemper, and Gregory L. Wagner. I would also like to thank Gregory L. Wagner
696 and an anonymous reviewer for their constructive comments. This work is supported by the
697 National Natural Science Foundation of China (42206031), a grant from the Research Grants
698 Council of the Hong Kong Special Administrative Region, China (AoE/P-601/23-N), and the
699 Guangdong Provincial Project (2023QN10H423). NCAR LES simulations presented in this work
700 were performed using computational resources at the Earth and Environmental Systems Research
701 Facility of the Hong Kong University of Science and Technology (Guangzhou).

702 *Data availability statement.* The source code and scripts for reproducing the test cases and
703 analyses in this work are archived at <https://doi.org/10.5281/zenodo.15104455>.

704 References

- 705 Beare, R. J., and Coauthors, 2006: An intercomparison of large-eddy simulations of the sta-
706 ble boundary layer. *Boundary-Layer Meteorology*, **118** (2), 247–272, <https://doi.org/10.1007/s10546-004-2820-6>.
- 708 Bühler, O., 2014: *Waves and Mean Flows*. Second edition ed., Cambridge Monographs on Me-
709 chanics, Cambridge University Press, Cambridge, United Kingdom ; New York.
- 710 Cox, S. M., and S. Leibovich, 1994: Large-scale Langmuir circulation and double-diffusive
711 convection: Evolution equations and flow transitions. *Journal of Fluid Mechanics*, **276**, 189–
712 210, <https://doi.org/10.1017/S0022112094002521>.
- 713 Craik, A. D. D., 1982: The drift velocity of water waves. *Journal of Fluid Mechanics*, **116**,
714 187–205, <https://doi.org/10.1017/s0022112082000421>.
- 715 Craik, A. D. D., and S. Leibovich, 1976: A rational model for Langmuir circulations. *Journal of*
716 *Fluid Mechanics*, **73** (03), 401–426, <https://doi.org/10.1017/S0022112076001420>.
- 717 D’Asaro, E. A., 2014: Turbulence in the upper-ocean mixed layer. *Annual Review of Marine*
718 *Science*, **6**, 101–15, <https://doi.org/10.1146/annurev-marine-010213-135138>.

- 719 D'Asaro, E. A., J. Thomson, A. Y. Shcherbina, R. R. Harcourt, M. F. Cronin, M. A. Hemer, and
720 B. Fox-Kemper, 2014: Quantifying upper ocean turbulence driven by surface waves. *Geophysical*
721 *Research Letters*, **41** (1), 102–107, <https://doi.org/10.1002/2013GL058193>.
- 722 Deardorff, J. W., 1980: Stratocumulus-capped mixed layers derived from a three-dimensional
723 model. *Boundary-Layer Meteorology*, **18** (4), 495–527, <https://doi.org/10.1007/BF00119502>.
- 724 Fan, X., B. Fox-Kemper, N. Suzuki, Q. Li, P. Marchesiello, P. P. Sullivan, and P. S. Hall, 2024:
725 Comparison of the Coastal and Regional Ocean COmmunity model (CROCO) and NCAR-
726 LES in non-hydrostatic simulations. *Geoscientific Model Development*, **17** (10), 4095–4113,
727 <https://doi.org/10.5194/gmd-17-4095-2024>.
- 728 Fan, Y., and S. M. Griffies, 2014: Impacts of parameterized langmuir turbulence and non-
729 breaking wave mixing in global climate simulations. *Journal of Climate*, **27** (12), 4752–4775,
730 <https://doi.org/10.1175/JCLI-D-13-00583.1>.
- 731 Fujiwara, Y., Y. Yoshikawa, and Y. Matsumura, 2020: Wave-resolving simulations of viscous wave
732 attenuation effects on Langmuir circulation. *Ocean Modelling*, **154**, 101 679, <https://doi.org/10.1016/j.ocemod.2020.101679>.
- 733 Garwood, R. W., P. C. Gallacher, and P. Muller, 1985: Wind Direction and Equilibrium Mixed Layer
734 Depth: General Theory. *Journal of Physical Oceanography*, **15** (10), 1325–1331, [https://doi.org/10.1175/1520-0485\(1985\)015<1325:wdaeml>2.0.co;2](https://doi.org/10.1175/1520-0485(1985)015<1325:wdaeml>2.0.co;2).
- 735 Gerkema, T., and V. I. Shrira, 2005: Near-inertial waves in the ocean: Beyond the ‘tradi-
736 tional approximation’. *Journal of Fluid Mechanics*, **529**, 195–219, <https://doi.org/10.1017/S0022112005003411>.
- 737 Grant, A. L. M., and S. E. Belcher, 2009: Characteristics of Langmuir turbulence in the ocean
738 mixed layer. *Journal of Physical Oceanography*, **39** (8), 1871–1887, <https://doi.org/10.1175/2009JPO4119.1>.
- 739 Hamlington, P. E., L. P. Van Roekel, B. Fox-Kemper, K. Julien, and G. P. Chini, 2014: Langmuir-
740 submesoscale interactions: Descriptive analysis of multiscale frontal spindown simulations.
741 *Journal of Physical Oceanography*, **44** (9), 2249–2272, <https://doi.org/10.1175/JPO-D-13-0139.1>.

- 747 Haney, S., B. Fox-Kemper, K. Julien, and A. Webb, 2015: Symmetric and geostrophic instabilities
748 in the wave-forced ocean mixed layer. *Journal of Physical Oceanography*, **45** (12), 3033–3056,
749 <https://doi.org/10.1175/JPO-D-15-0044.1>.
- 750 Harcourt, R. R., 2013: A second-moment closure model of Langmuir turbulence. *Journal of*
751 *Physical Oceanography*, **43** (4), 673–697, <https://doi.org/10.1175/JPO-D-12-0105.1>.
- 752 Harcourt, R. R., and E. A. D'Asaro, 2008: Large-eddy simulation of Langmuir turbulence in
753 pure wind seas. *Journal of Physical Oceanography*, **38** (7), 1542–1562, <https://doi.org/10.1175/2007JPO3842.1>.
- 755 Holm, D. D., 1996: The ideal Craik-Leibovich equations. *Physica D: Nonlinear Phenomena*,
756 **98** (2-4), 415–441, [https://doi.org/10.1016/0167-2789\(96\)00105-4](https://doi.org/10.1016/0167-2789(96)00105-4).
- 757 Huang, J., M. Chamecki, Q. Li, and B. Chen, 2026: The role of longitudinal alignment between
758 surface and bottom forcing on the full-column turbulence mixing in the coastal ocean. *Ocean*
759 *Modelling*, **199**, 102637, <https://doi.org/10.1016/j.ocemod.2025.102637>.
- 760 Kukulka, T., A. J. Plueddemann, J. H. Trowbridge, and P. P. Sullivan, 2009: Significance of
761 Langmuir circulation in upper ocean mixing: Comparison of observations and simulations.
762 *Geophysical Research Letters*, **36** (10), L10603, <https://doi.org/10.1029/2009GL037620>.
- 763 Kukulka, T., A. J. Plueddemann, J. H. Trowbridge, and P. P. Sullivan, 2011: The influence of
764 crosswind tidal currents on Langmuir circulation in a shallow ocean. *Journal of Geophysical*
765 *Research: Oceans*, **116** (C8), C08005, <https://doi.org/10.1029/2011JC006971>.
- 766 Large, W. G., E. G. Patton, A. K. DuVivier, P. P. Sullivan, and L. Romero, 2019: Similarity
767 theory in the surface layer of large-eddy simulations of the wind, wave and buoyancy forced
768 Southern Ocean. *Journal of Physical Oceanography*, **49** (8), 2165–2187, <https://doi.org/10.1175/JPO-D-18-0066.1>.
- 770 Leibovich, S., 1977: Convective instability of stably stratified water in the ocean. *Journal of Fluid*
771 *Mechanics*, **82**, 561–581, <https://doi.org/10.1017/S0022112077000846>.
- 772 Leibovich, S., 1983: The form and dynamics of Langmuir circulations. *Annual Review of Fluid*
773 *Mechanics*, **15**, 391–427.

- 774 Leibovich, S., and S. K. Lele, 1985: The influence of the horizontal component of Earth's
775 angular velocity on the instability of the Ekman layer. *Journal of Fluid Mechanics*, **150**, 41–87,
776 <https://doi.org/10.1017/S0022112085000039>.
- 777 Leibovich, S., S. K. Lele, and I. M. Moroz, 1989: Nonlinear dynamics in Langmuir circulations
778 and in thermosolutal convection. *Journal of Fluid Mechanics*, **198**, 471–511, <https://doi.org/>
779 [10.1017/S0022112089000224](https://doi.org/10.1017/S0022112089000224).
- 780 Li, M., C. Garrett, and E. D. Skyllingstad, 2005: A regime diagram for classifying turbulent large
781 eddies in the upper ocean. *Deep-Sea Research Part I: Oceanographic Research Papers*, **52 (2)**,
782 259–278, <https://doi.org/10.1016/j.dsr.2004.09.004>.
- 783 Li, Q., and B. Fox-Kemper, 2017: Assessing the effects of Langmuir turbulence on the entrainment
784 buoyancy flux in the ocean surface boundary layer. *Journal of Physical Oceanography*, **47 (12)**,
785 2863–2886, <https://doi.org/10.1175/JPO-D-17-0085.1>.
- 786 Li, Q., and B. Fox-Kemper, 2020: Anisotropy of Langmuir turbulence and the Langmuir-
787 enhanced mixed layer entrainment. *Physical Review Fluids*, **5 (1)**, 013803, <https://doi.org/>
788 [10.1103/PhysRevFluids.5.013803](https://doi.org/10.1103/PhysRevFluids.5.013803).
- 789 Li, Q., A. Webb, B. Fox-Kemper, A. Craig, G. Danabasoglu, W. G. Large, and M. Vertenstein, 2016:
790 Langmuir mixing effects on global climate: WAVEWATCH III in CESM. *Ocean Modelling*,
791 **103**, 145–160, <https://doi.org/10.1016/j.ocemod.2015.07.020>.
- 792 Li, Q., and Coauthors, 2019: Comparing ocean surface boundary vertical mixing schemes including
793 Langmuir turbulence. *Journal of Advances in Modeling Earth Systems*, **11 (11)**, 3545–3592,
794 <https://doi.org/10.1029/2019MS001810>.
- 795 Liu, J., J.-H. Liang, J. C. McWilliams, P. P. Sullivan, Y. Fan, and Q. Chen, 2018: Effect of planetary
796 rotation on oceanic surface boundary layer turbulence. *Journal of Physical Oceanography*, **48 (9)**,
797 2057–2080, <https://doi.org/10.1175/JPO-D-17-0150.1>.
- 798 Longuet-Higgins, M. S., 1953: Mass Transport in Water Waves. *Philosophical Transactions of
799 the Royal Society of London A: Mathematical, Physical and Engineering Sciences*, **245 (903)**,
800 535–581, <https://doi.org/10.1098/rsta.1953.0006>.

- 801 McWilliams, J. C., E. Huckle, J.-H. Liang, and P. P. Sullivan, 2012: The wavy Ekman layer:
802 Langmuir circulations, breaking waves, and Reynolds stress. *Journal of Physical Oceanography*,
803 **42** (11), 1793–1816, <https://doi.org/10.1175/JPO-D-12-07.1>.
- 804 McWilliams, J. C., E. Huckle, J.-H. Liang, and P. P. Sullivan, 2014: Langmuir turbulence in swell.
805 *Journal of Physical Oceanography*, **44** (3), 870–890, <https://doi.org/10.1175/JPO-D-13-0122.1>.
- 806 McWilliams, J. C., and J. M. Restrepo, 1999: The wave-driven ocean circulation. *Journal of
807 Physical Oceanography*, **29** (10), 2523–2540, [https://doi.org/10.1175/1520-0485\(1999\)029%3C2523:TWDOC%3E2.0.CO;2](https://doi.org/10.1175/1520-0485(1999)029%3C2523:TWDOC%3E2.0.CO;2).
- 808 McWilliams, J. C., P. P. Sullivan, and C.-H. Moeng, 1997: Langmuir turbulence in the ocean.
809 *Journal of Fluid Mechanics*, **334** (1), 1–30, <https://doi.org/10.1017/S0022112096004375>.
- 810 Moeng, C.-H., 1984: A large-eddy-simulation model for the study of planetary boundary-layer
811 turbulence. *Journal of the Atmospheric Sciences*, **41** (13), 2052–2062, [https://doi.org/10.1175/1520-0469\(1984\)041<2052:ALESMF>2.0.CO;2](https://doi.org/10.1175/1520-0469(1984)041<2052:ALESMF>2.0.CO;2).
- 812 Pearson, B., 2018: Turbulence-induced anti-Stokes flow and the resulting limitations of large-
813 eddy simulation. *Journal of Physical Oceanography*, **48** (1), 117–122, <https://doi.org/10.1175/JPO-D-17-0208.1>.
- 814 Polton, J. A., D. M. Lewis, and S. E. Belcher, 2005: The role of wave-induced Coriolis-Stokes
815 forcing on the wind-driven mixed layer. *Journal of Physical Oceanography*, **35**, 444–457,
816 <https://doi.org/10.1175/JPO2701.1>.
- 817 Ramadhan, A., and Coauthors, 2020: Oceananigans.jl: Fast and friendly geophysical fluid dy-
818 namics on GPUs. *Journal of Open Source Software*, **5** (53), 2018, <https://doi.org/10.21105/joss.02018>.
- 819 Rozema, W., H. J. Bae, P. Moin, and R. Verstappen, 2015: Minimum-dissipation models for
820 large-eddy simulation. *Physics of Fluids*, **27** (8), 085107, <https://doi.org/10.1063/1.4928700>.
- 821 Shrestha, K., W. Anderson, A. Tejada-Martinez, and J. Kuehl, 2019: Orientation of coastal-zone
822 Langmuir cells forced by wind, wave and mean current at variable obliquity. *Journal of Fluid
823 Mechanics*, **879**, 716–743, <https://doi.org/10.1017/jfm.2019.683>.

- 828 Sullivan, P. P., and J. C. McWilliams, 2010: Dynamics of winds and currents coupled to
829 surface waves. *Annual Review of Fluid Mechanics*, **42** (1), 19–42, <https://doi.org/10.1146/annurev-fluid-121108-145541>.
- 831 Sullivan, P. P., and J. C. McWilliams, 2024: Oceanic frontal turbulence. *Journal of Physical*
832 *Oceanography*, **54** (2), 333–358, <https://doi.org/10.1175/JPO-D-23-0033.1>.
- 833 Sullivan, P. P., J. C. McWilliams, and C.-h. Moeng, 1994: A subgrid-scale model for large-eddy
834 simulation of planetary boundary-layer flows. *Boundary-Layer Meteorology*, **71**, 247–276.
- 835 Sullivan, P. P., L. Romero, J. C. McWilliams, and W. K. Melville, 2012: Transient evolution of
836 Langmuir turbulence in ocean boundary layers driven by hurricane winds and waves. *Journal of*
837 *Physical Oceanography*, **42**, 1959–1980, <https://doi.org/10.1175/JPO-D-12-025.1>.
- 838 Suzuki, N., and B. Fox-Kemper, 2016: Understanding Stokes forces in the wave-averaged
839 equations. *Journal of Geophysical Research: Oceans*, **121** (5), 3579–3596, <https://doi.org/10.1002/2015JC011566>.
- 841 Suzuki, N., B. Fox-Kemper, P. E. Hamlington, and L. P. Van Roekel, 2016: Surface waves affect
842 frontogenesis. *Journal of Geophysical Research: Oceans*, **121** (5), 3597–3624, <https://doi.org/10.1002/2015JC011563>.
- 844 Teixeira, M. A. C., 2011: A linear model for the structure of turbulence beneath surface water
845 waves. *Ocean Modelling*, **36** (1–2), 149–162, <https://doi.org/10.1016/j.ocemod.2010.10.007>.
- 846 Thorpe, S. A., 2004: Langmuir circulation. *Annual Review of Fluid Mechanics*, **36** (1), 55–79,
847 <https://doi.org/10.1146/annurev.fluid.36.052203.071431>.
- 848 Tort, M., and K. B. Winters, 2018: Poleward propagation of near-inertial waves induced by
849 fluctuating winds over a baroclinically unstable zonal jet. *Journal of Fluid Mechanics*, **834**,
850 510–530, <https://doi.org/10.1017/jfm.2017.698>.
- 851 Tsai, W.-t., G.-h. Lu, J.-r. Chen, A. Dai, and W. R. C. Phillips, 2017: On the formation of
852 coherent vortices beneath nonbreaking free-propagating surface waves. *Journal of Physical*
853 *Oceanography*, **47** (3), 533–543, <https://doi.org/10.1175/JPO-D-16-0242.1>.

- 854 Van Roekel, L., B. Fox-Kemper, P. P. Sullivan, P. E. Hamlington, and S. R. Haney, 2012: The
855 form and orientation of Langmuir cells for misaligned winds and waves. *Journal of Geophysical*
856 *Research*, **117 (C05001)**, C05 001, <https://doi.org/10.1029/2011JC007516>.
- 857 Verstappen, R., 2018: How much eddy dissipation is needed to counterbalance the nonlinear
858 production of small, unresolved scales in a large-eddy simulation of turbulence? *Computers &*
859 *Fluids*, **176**, 276–284, <https://doi.org/10.1016/j.compfluid.2016.12.016>.
- 860 Wagner, G. L., G. P. Chini, A. Ramadhan, B. Gallet, and R. Ferrari, 2021: Near-inertial waves and
861 turbulence driven by the growth of swell. *Journal of Physical Oceanography*, **51 (5)**, 1337–1351,
862 <https://doi.org/10.1175/JPO-D-20-0178.1>.
- 863 Wagner, G. L., and N. C. Constantinou, 2025: Phenomenology of decaying turbulence beneath
864 surface waves. *Journal of Fluid Mechanics*, **1020**, A51, <https://doi.org/10.1017/jfm.2025.10649>.
- 865 Wagner, G. L., N. Pizzo, L. Lenain, and F. Veron, 2023: Transition to turbulence in wind-drift
866 layers. *Journal of Fluid Mechanics*, **976**, A8, <https://doi.org/10.1017/jfm.2023.920>.
- 867 Wang, D., 2006: Effects of the earth's rotation on convection: Turbulent statistics, scaling laws and
868 Lagrangian diffusion. *Dynamics of Atmospheres and Oceans*, **41 (2)**, 103–120, <https://doi.org/10.1016/j.dynatmoce.2006.01.001>.
- 870 Wang, D., T. Kukulka, B. G. Reichl, T. Hara, and I. Ginis, 2019: Wind-Wave Misalignment Effects
871 on Langmuir Turbulence in Tropical Cyclones Conditions. *Journal of Physical Oceanography*,
872 **49 (12)**, 3109–3126, <https://doi.org/10.1175/JPO-D-19-0093.1>.
- 873 Wei, Z., Q. Li, and B. Chen, 2025: A direct assessment of Langmuir turbulence parameterizations
874 in idealized coastal merging boundary layers. *Journal of Advances in Modeling Earth Systems*,
875 under Review.